| | |
|---|---|
| Title | Structural studies on the stalk region of the dynein motor domain |
| Author(s) | 西河，洋祐 |
| Citation | 大阪大学，2014，博士論文 |
| Version Type | VoR |
| URL | https://doi.org/10.18910/52269 |
| rights | |
| Note | |

# Structural studies on the stalk region of the dynein motor domain
# (ダイニンモータードメインにあるストーク領域の構造研究)

A Doctoral Thesis
By
Yosuke Nishikawa

Submitted to the Graduate School of Science,
Osaka University
Japan

November, 2014

## Acknowledgement

This study has been carried out under the direction of Professor Genji Kurisu of Institute for Protein Research, Osaka University. I would like to express the deepest appreciation to him for incessant guidance and encouragement throughout this work.

I am deeply grateful to Assistant Professor Takuji Oyama of University of Yamanashi for appropriate advice and support about crystal handling and whole of crystallographic analysis. It was impossible for me to have completed this work without his enormous contribution. I would like to thank Associate Professor Narutoshi Kamiya and Professor Haruki Nakamura of Institute for Protein Research, Osaka University for precise feedback and enormous support for molecular dynamics simulations. I am also grateful Professor Takahide Kon of Hosei University for kindly advice and helpful suggestion. My heartfelt appreciation goes to Professor Yoko Yano-Toyoshima of the University of Tokyo for constructive discussion and sincere encouragement.

I am also deeply grateful to Professor Atsushi Nakagawa of Institute for Protein Research, Osaka University and Professor Katsumi Imada of Osaka University for reviewing manuscript and appropriate advice.

I am also deeply grateful to Assistant Professor Hisashi Yagi of Tottori University and Professor Yuji Goto, Dr. Masatomo So and Dr. Young-Ho Lee of Institute for Protein Research, Osaka University for support with CD measurement.

I am also deeply grateful to Assistant Professor Eiki Yamashita, Assistant Professor Akifumi Higashiura of Institute for Protein Research, Osaka University and Associate Professor Yasuhumi Umena of Osaka City University for technical advice about X-ray data collection.

I would like to express my gratitude to Dr. Etsuko Muto and Dr. Seiichi Uchimura of Brain Science Institute, RIKEN.

I also wish to thank Mr. Hisaaki Osako, Ms. Momoko Inatomi and Ms. Haruka Iwasaki for their huge contribution to sample preparation and protein crystallization.

I want to thank all members in Kurisu’s laboratory for their helpful support and scientific stimulation.

Finally, I would like to thank my parents for their patience and support.

November 2014

西河浄祐

**Yosuke Nishikawa**
Department of Macromolecular Science
the Graduate School of Science
Osaka University

# Table of contents

## Chapter 3

## Structure and Function of the dynein stalk region

## Chapter 4

## General discussion

## Chapter 5

## Summary

## References

## List of publications

## Abbreviation

| | |
|---|---|
| $AAA^+$ | ATPases associated with diverse cellular activities |
| AC | artificial coiled coil |
| AMP-PNP | 5’-adenylyl-β-γ-imidodiphosphate |
| Bcr | coiled-coil structure of Bcr-Abl protein |
| CD | circular dichroism |
| DTT | dithiothreitol |
| EDTA | ethylenediamine-N,N,N', N'-tetraacetic Acid |
| EM | Electron microscope |
| IPTG | isopropyl β-D-1-thiogalactopyranoside |
| MAD | multi-wavelength anomalous dispersion method |
| SAD | single-wavelength anomalous dispersion method |
| MD | molecular dynamics |
| MPD | 2-Methyl-2,4-pentanediol |
| MT | microtubule |
| MTBD | microtubule-binding domain |
| PAGE | polyacrylamide gel electrophoresis |
| PEG | polyethylene glycol |
| PMSF | phenylmethylsulfonyl fluoride |
| SeMet | Seleno-L-Methionine |
| SRS | seryl-tRNA synthetase |
| Tris | tris(hydroxymethyl)aminomethane |
| Vi | orthovanadate |

# Chapter 1

# 1. Introduction

## 1.1 Cytoskeletal motors

Eukaryotic cells utilize several kinds of motors for essential cellular activities. They generate kinetic force by ATP hydrolysis, and drive cell migration, intracellular transport, cilia and flagellar beating and so on [Vale, 2003; DiBella, 2001]. Myosin, kinesin and dynein are known as the major groups of these linear motor proteins. These motors use different track systems. Myosin moves along actin filaments while kinesin and dynein families move on the microtubule filaments [Mallik, 2004].

To perform motor activities, following three points are necessary for motor proteins; 1) ATP hydrolysis, 2) force generation and 3) track binding. In the cases of kinesin and myosin, a head domain is responsible for ATP hydrolysis and track binding. Neck domain of kinesin or lever-arm domain of myosin adjacent to the head domain generates kinetic force (**Figure 1.1**) [Coureux *et al.*, 2003; Kozielski *et al.* 1997]. In the case of dynein, functional domains are clearly separated as independent structural domains. ATP is hydrolyzed at ATP hydrolyzing domain called "AAA ring", kinetic force is generated by a linker domain and microtubule-binding is mediated by a microtubule-binding domain called MTBD (**Figure 1.2**) [Asai *et al.*, 2001; Mizuno *et al.*, 2007].

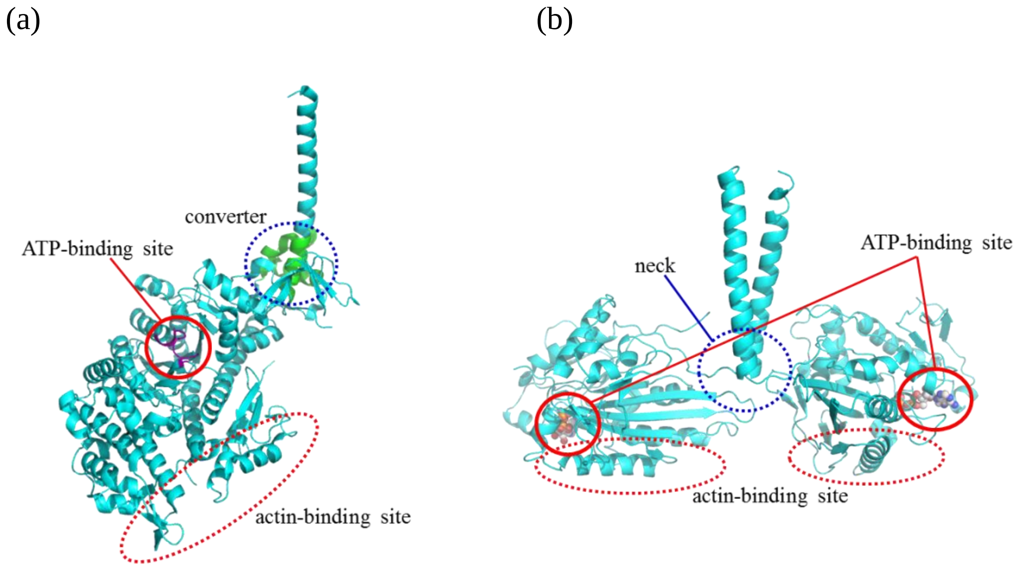

**Figure 1.1 Crystal structures of cytoskeletal motor**

(a) Crystal structure of myosinV (PDB ID : 1OE9)

(b) Crystal structure of kinesin dimer (PDB ID : 3KIN)

This figure was created using Pymol software [DeLano, 2002].

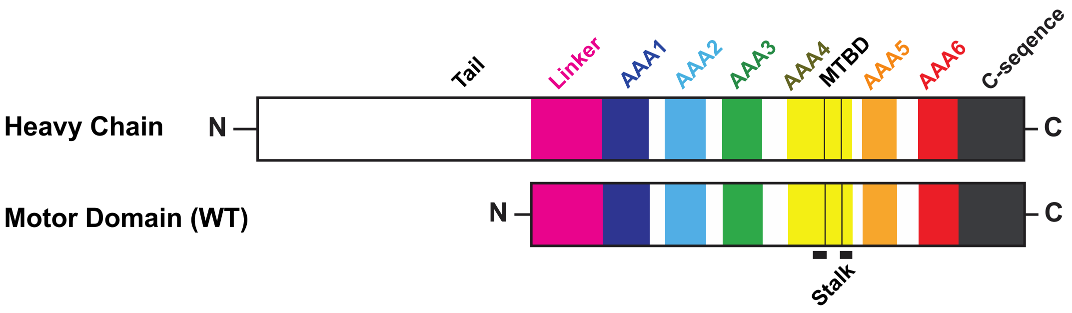

**Figure 1.2 Sequence diagram of the dynein motor domain**

This diagram shows the functional units: the linker, the ring containing six $AAA^+$ modules, the microtubule-binding domain (MTBD) and the C-sequence [Koonce *et al*., 1996]. At the bottom of the diagram, the location of the stalk region is indicated.

## 1.2 Dyneins

### 1.2.1 Functions of dynein

Dynein is microtubule based motor protein. It moves along microtubules toward their minus end and its energy resource is ATP hydrolysis as described above. There are two major classes of dynein. Cytoplasmic dynein is involved in nuclear segregation, cell mitosis, and translocation of various cargo and intracellular organelles [Karki *et al.*, 1999]. The other one is axonemal dynein, which drives the beating of flagella and the motions of cilia [Gibbons, 1981; DiBella *et al.*, 2001]. These functions are essential for eukaryotic cells and its defections lead to severe disorders. Defects of cytoplasmic dynein bring on neurodegenerative diseases such as amyotrophic lateral sclerosis (ALS), spinal-bulbar muscular atrophy (SBMA), and spinal muscular atrophy (SMA) because of inhibitions of axonal transport in neural cells [Hafezparast *et al.*, 2003]. Also disassembly of axonemal dynein raises severe disorders of the liver and pancreas, diabetes, obesity and skeletal dysplasia. The series of axonemal dynein-dependent diseases are called ciliopathy [Waters *et al.*, 2011]. To reveal the mechanism of dynein movement will provide basic knowledge of cellar activities closely related to these diseases.

### 1.2.2 Stepping mechanism of dynein

To move on the cytoskeletons, motor proteins require precise coordination of ATP hydrolysis, generation of mechanical force and track-binding activities. The relationships between a catalytic cycles of ATP hydrolysis, linker swing and track binding of MTBD are revealed from biochemical experiments of Walker motif mutants and FRET experiments of recombinant dynein variants with inserted fluorescent proteins [Burgess *et al.*, 2003; Höök *et al.*, 2005; Kon *et al.*, 2005; Roberts *et al.*, 2009]. The step sequence of dynein movement is stated as below; 1) Microtubule-binding of dynein accelerates ATP hydrolysis. 2) Binding of ATP to dynein induces dissociation between MTBD and microtubule. 3) Dissociation from MT induce “recovery stroke” of the linker and ready to pull the cargoes. 4) Recovery stroke induce ATP hydrolysis. 4)

After ATP hydrolysis, dynein release the phosphate and re-bind to microtubule. 5) Then the linker swings as “power stroke” and 6) release the ADP following the state waiting a next nucleotide binding (**Figure 1.3**).

To achieve this stepping cycle, each domain should communicate with the others. The track binding MTBD is structurally separated about 15 nm from the nucleotide binding site by stalk coiled coil. So a long-range communication is necessary between them. Recently this intramolecular communication is explained by “Helix-sliding model”, in which the signal transmission of ATP hydrolysis and binding to microtubule is mediated by an alignment change between two helices in the stalk coiled coil. Helix sliding model was first confirmed by Gibbons and his colleagues in 2005. They fused mouse dynein stalk region with different coiled-coil registries onto *Thermus thermophilus* seryl-tRNA synthetase (SRS) as a stable coiled coil base to fix the coiled-coil registry (**Figure 1.4**). These constructs were tested for microtubule binding by co-sedimentation assay. In consequence, affinities to microtubule were dependent on alignment of helices of each construct and only one specific alignment, called α registry exhibits high affinity [Gibbons *et al*., 2005]. In 2009 Kon and his colleagues have corroborated helix-sliding model by utilizing cysteine double mutants of dynein motor domain whose registries of the stalk coiled coil were fixed by disulfide bond. Locking the registry of engineered dynein motor domain did not couple the ATP hydrolysis with the microtubule binding activities. The three different registries of +β, α and -β were tested in this report (**Figure 1.4**). The mutant protein of α registry exhibited high ATPase activity and high affinity to microtubule. Conversely, the +β one showed low ATPase activity and low affinity, and the –β one showed high ATPase activity and low affinity to microtubule [Kon *et al*., 2009]. These results imply that registry of the stalk coiled coil keeps changing during stepping process. The stalk coiled coil in +β registry corresponds to the D-ATP and the D*-ATP states, while that in α registry to the other states. (**Figures 1.3 and 1.4**)

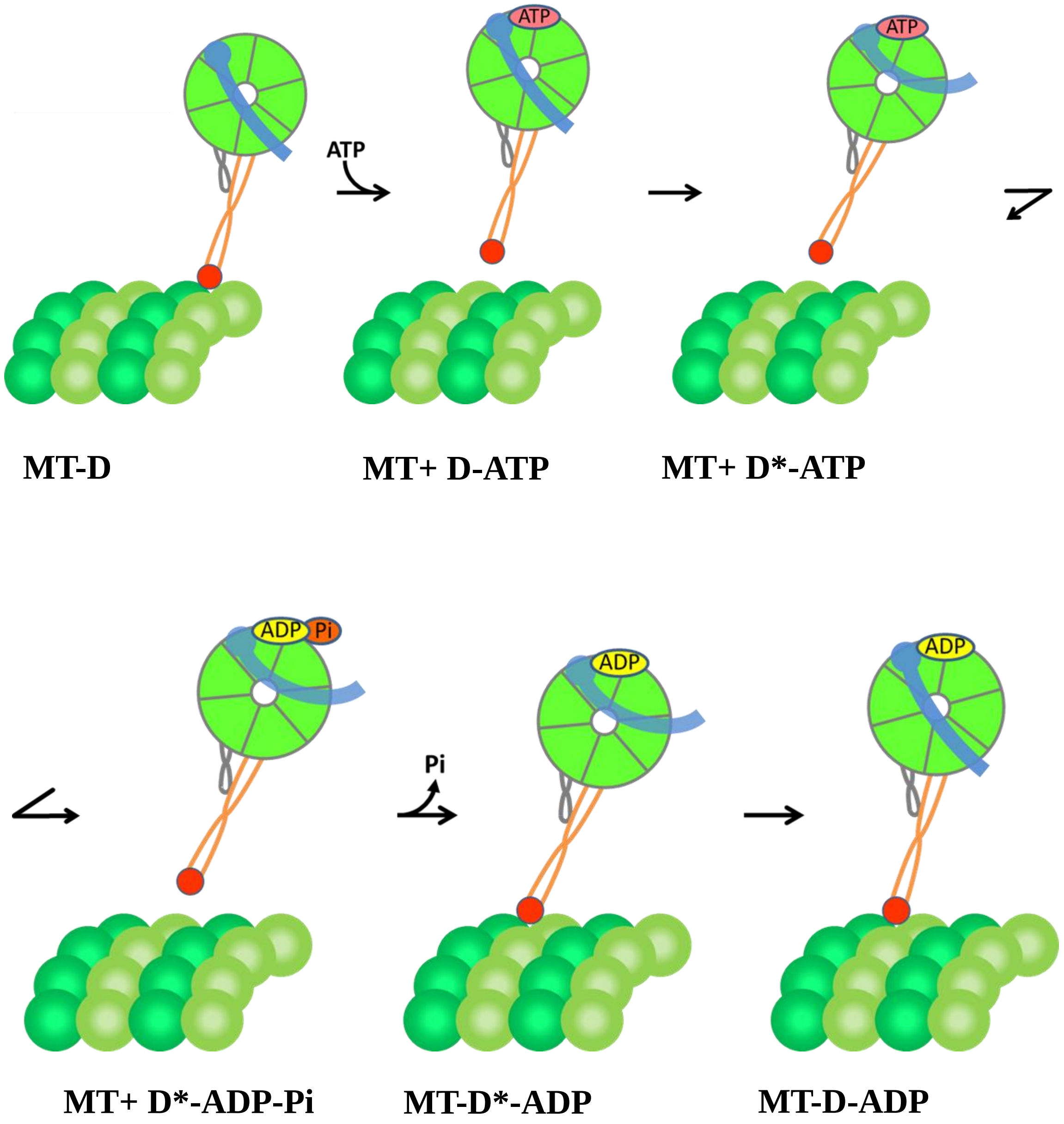

**Figure 1.3 Schematic view of dynein stepping cycle.**

See the text of section 1.2.2 in detail.

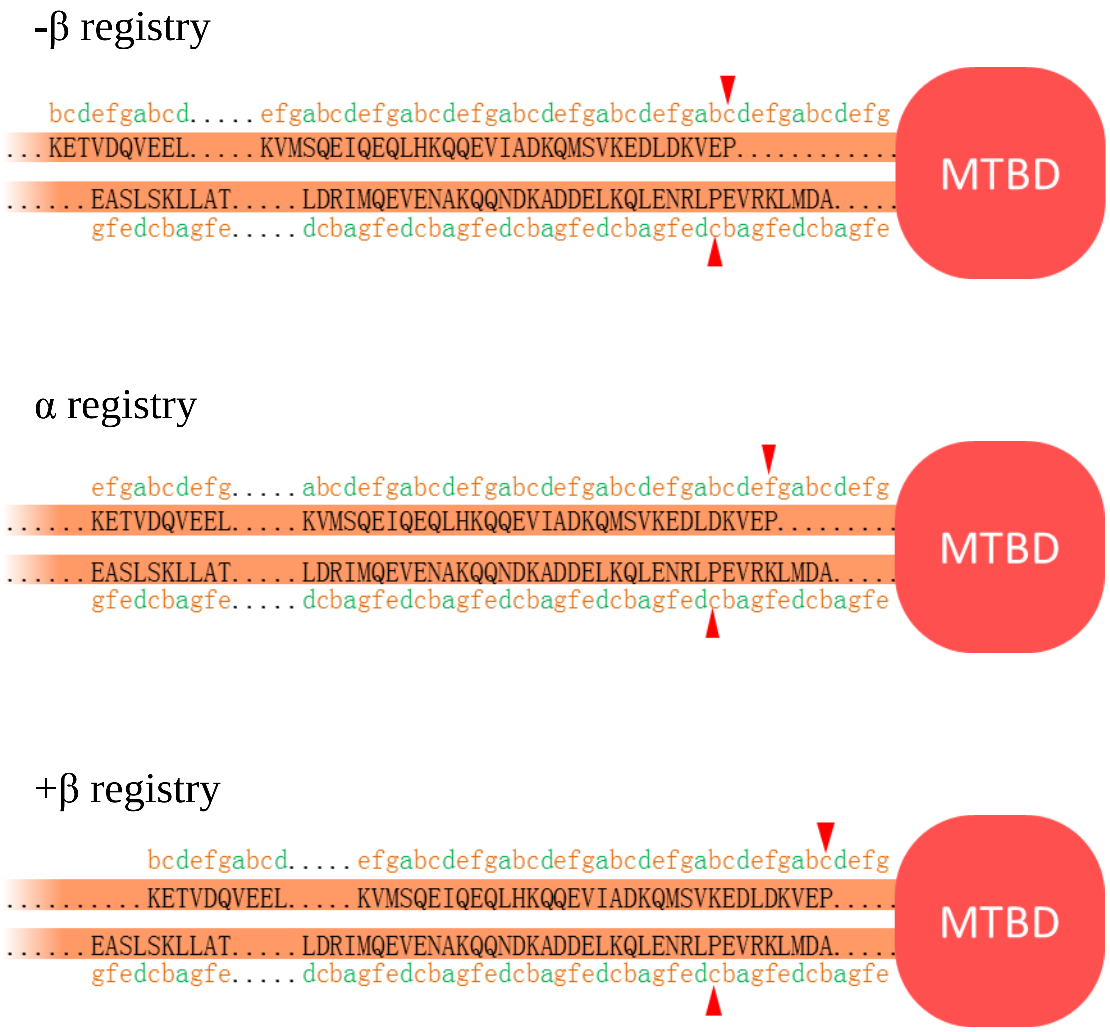

**Figure 1.4 Example of registries in mouse dynein stalk region**

Three different heptad coiled coil registries are shown based on the mouse dynein sequence. Conserved two proline residues are indicated by red allowheads.

### 1.2.3 Previous structural studies on dynein

Both classes of dyneins have unique features standing out from other motor proteins. They belongs to AAA$^+$ superfamily (ATPases associated with diverse cellular activities) [Kunau *et al*., 1993; Neuwald *et al*., 1999], while kinesin and myosin are commonly originated from a G protein [Kull *et al*., 1996 & 1998]. Dynein is a large motor complex (over 1000 kDa) compared with kinesin (conventional kinesin ~40 kDa) and myosin (myosin V ~80 kDa). The dynein complex is made up of heavy, intermediate and light chains. Among these three chains, the heavy chain is responsible for motile activity and its functional core is called the motor domain. This domain comprises an N-terminal linker (i.e., the mechanical element), a central ring of six AAA$^+$ modules (four of which bind or hydrolyze ATP), and a long stalk connected to a microtubule binding domain (MTBD) at its tip extending from the fourth module of the AAA$^+$ ring. The domain organization of dynein was initially revealed by electron microscopic analysis [Sakakibara *et al*., 1999; Burgess *et al*., 2003; Roberts *et al*., 2009] and recently by X-ray crystallographic analysis of dynein motor domains [Carter *et al*., 2011; Kon *et al*., 2011&2012; Schmidt *et al*., 2012].

The first X-ray structure of dynein was acquired by analysis of the MTBD fused with SRS in a weak microtubule-binding form with the heptad repeat of the stalk coiled coil fixed in the +β registry. The microtubule-binding surface of dynein and the heptad registry were determined at 2.3 Å resolution [Carter *et al*., 2008]. However, the SRS-MTBD fusion protein in a strong microtubule-binding form has not yet been crystallized. Quite recently, a pseudoatomic resolution structure of the SRS-MTBD bound to the microtubule was determined using cryo-TEM reconstruction at 9.7 Å resolution and molecular dynamics simulations [Redwine *et al*., 2012]. The initial model, which was revealed by the SRS-MTBD structure in a weak microtubule-binding form, agreed well within the experimental density, although the coiled coil remained in the low-affinity registry of +β. The final model with the half-heptad registry shift from +β to α was obtained by applying targeted molecular dynamics. On the basis of these initial and fitted structures, a large displacement of the H1 helix within the MTBD and an opening of CC1 helix at the base of the stalk are proposed as required for the structural reorganization that determines the registry change from a weak (+β) to a strong microtubule binding mode (α).

Functional analysis of the recombinant 380-kDa motor domain of cytoplasmic dynein from *Dictyostelium discoideum* revealed the relationships between stalk conformation, ATPase, and microtubule binding activities [Kon *et al*., 2009]. Together with this functional analysis, X-ray structures are available for the ADP-bound form of the wild-type and the ΔMTBD dynein motor domain from *D. discoideum* at 3.8 Å and 2.8 Å resolution, respectively (Figure 1.4) [Kon *et al*., 2012]. These structures show that the entire portion of the stalk region is in the strong microtubule-binding form, i.e., the heptad repeat is in the α registry, however they lack the distal portion of stalk region due to disordered electron density and truncation of MTBD.

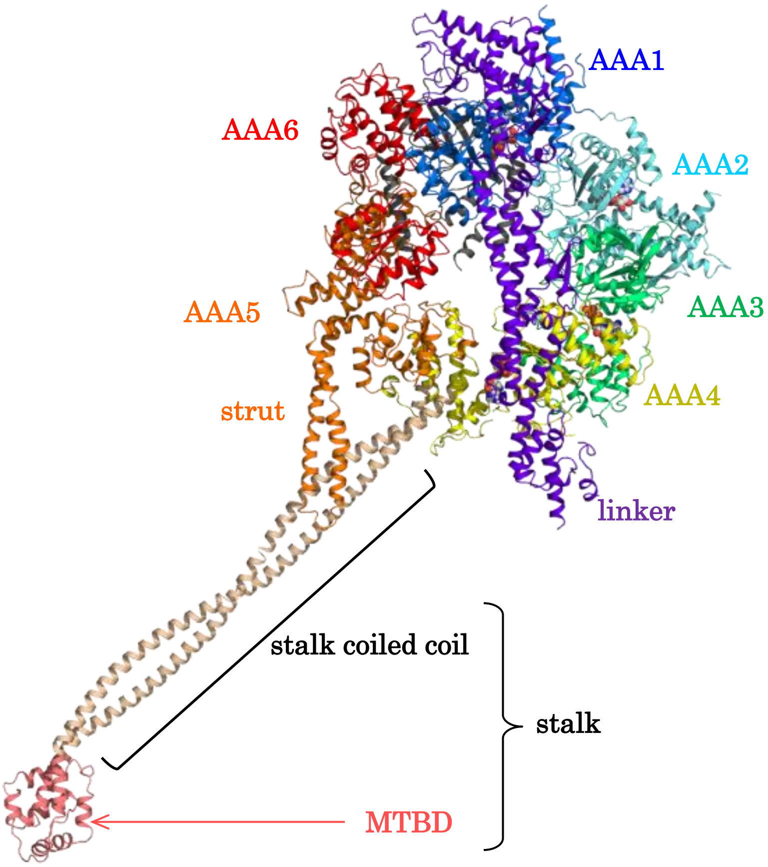

**Figure 1.5 Hypothetical complete structure of dynein motor domain**

Hypothetical structure of full-length dynein motor domain based on the crystal structure of dynein motor domain from *D. discoideum* (PDB ID : 3VKG) and dynein stalk (PDB ID : 3WUQ)

### 1.3 Purpose of this study

Despite these unambiguous results from functional studies, the structural basis for the helix-sliding mechanism is poorly understood, and two fundamental issues remain to be resolved. First, a high-resolution structure of the SRS-MTBD fusion protein includes only a small portion of the stalk coiled coil [Carter *et al.*, 2008]. Therefore, it cannot be determined whether the remainder of the coiled coil forms a canonical coiled coil with a registry of +β through the entire stalk. Second, although the 3.8 Å structure of the ADP-bound form of the dynein motor domain includes the intact stalk region, the electron density of the distal portion of the CC1 coiled-coil helix is not sufficiently clear to model the coordinates. The complete structure of the dynein stalk is required to fully understand the structural basis for the helix-sliding mechanism through the entire stalk region. Indeed, the structure of the stalk region provides a good starting model for performing molecular dynamic simulations that might provide a structural basis to explain how the dynein stalk coordinates the action of the $AAA^+$ ring and the MTBD. Here, we have performed such a study by means of biophysical analysis of the entire portion of the microtubule-binding stalk.

# Chapter 2

## 2. Materials & Methods

### 2.1 Construction

*Escherichia coli* was used in expression of the dynein stalk domain. Expression constructs were engineered based on the pET System (Merck). Stalk regions of cytoplasmic dynein from *Mus musculus* and *Dictyostelium discoideum*, axonemal dynein from *Chlamydomonas reinhardtii* and *Homo sapiens* were picked up as sources for structural analysis (listed in **Table 2.1**). Basic design of these constructs is shown in **Figure 2.1**.

The target sequences encoding dynein stalk regions were amplified with additional C-terminal 6× His tag sequence or N-terminal 6× His tag combined with Factor Xa recognition site. To express the proteins in *E. coli*, amplified DNA fragments were engineered into the NdeI and EcoRI sites of pET-17b vector. The DNA sequence was verified by the dideoxy chain termination method by using BigDye terminator and 3130 Genetic Analyzer (ABI). Constructs and their design for disulfide cross linkage to fix the registry are shown in **Figure 2.2**, respectively.

To make the both terminal regions more stable, I also designed the chimeric construct fused with stable coiled coils. Artificial coiled coil (AC) [Yang *et al*., 2006] and bacterial coiled coil (Bcr) structures [Zhao *et al*., 2002], whose X-ray structures were available already were used as the base to ensure the stable coiled coil packing as shown in **Figure 2.3**.

In order to focus on the coiled coil region, the constructs without MTBD were designed in parallel. In these constructs, each registry is strictly fixed and there is no need to fix it by S-S linkage (**Figure 2.4**).

I also designed the relatively bigger construct including not only the stalk region but also adjacent AAA4 and AAA5 modules. *Escherichia coli* was used in expression of this construct. Since this construct is relatively big, the target sequence was introduced into the NdeI and HindIII of pCold-TF and expressed as a fusion protein with 6× His tag and Trigger factor for increase protein solubility and stability (**Figure 2.1b**).

In addition to structural analysis of stalk region itself, direct visualization of interactions between MTBD and microtubule in electron microscopic analysis were carried out by research collaborators Dr. Uchimura and Dr. Muto (Laboratory for Molecular Biophysics, Brain Science Institute, RIKEN). I provided several constructs as samples for EM analysis to them. Their article is submitted about interaction of MTBD and microtubule including EM analysis together with motility, microtubule binding and ATPase assay.

## Table. 2.1 Constructs in this work

| Name | Host | Source |
|---|---|---|
| AC-mDS-His | BL21(DE3) codon plus RIL | *Mus musculus*<br>cytoplasmic dynein |
| Bcr-mDS-His | BL21(DE3) codon plus RIL | *Mus musculus*<br>cytoplasmic dynein |
| mDS277-His | BL21(DE3) codon plus RIL | *Mus musculus*<br>cytoplasmic dynein |
| mDS277-His | B834(DE3) pLysS | *Mus musculus*<br>cytoplasmic dynein |
| mDS269-His | Rosetta2(DE3) | *Mus musculus*<br>cytoplasmic dynein |
| mDS262-His | BL21(DE3) | *Mus musculus*<br>cytoplasmic dynein |
| mDS277α-His | BL21(DE3) | *Mus musculus*<br>cytoplasmic dynein |
| mDS277ΔMTBD+β-His | Rosetta2(DE3) | *Mus musculus*<br>cytoplasmic dynein |
| mDS277ΔMTBDα-His | BL21(DE3) codon plus RIL | *Mus musculus*<br>cytoplasmic dynein |
| mDS277ΔMTBD-β-His | Rosetta2(DE3) | *Mus musculus*<br>cytoplasmic dynein |
| mDS277ΔMTBDα | BL21(DE3) codon plus RIL | *Mus musculus*<br>cytoplasmic dynein |
| dDS278-His | Rosetta2 (DE3) | *Dictyostelium discoideum*<br>cytoplasmic dynein |
| dDS278+β-His | Rosetta2 (DE3) | *Dictyostelium discoideum*<br>cytoplasmic dynein |
| dDS278α-His | Rosetta2 (DE3) | *Dictyostelium discoideum*<br>cytoplasmic dynein |
| dDS278-β-His | Rosetta2 (DE3) | *Dictyostelium discoideum*<br>cytoplasmic dynein |
| AC-dDS-His | BL21(DE3) codon plus RIL | *Dictyostelium discoideum*<br>cytoplasmic dynein |
| DHC8s289 | BL21(DE3) | *Chlamydomonas reinhardtii*<br>axenemal dynein |
| DHC9s288 | BL21(DE3) codon plus RIL | *Chlamydomonas reinhardtii*<br>axenemal dynein |
| DNAH7s291-His | Rosetta2(DE3) | *Homo sapiens*<br>axenemal dynein |
| His-TF-h4st5 | BL21(DE3) STAR | *Homo sapiens*<br>cytoplasmic dynein |

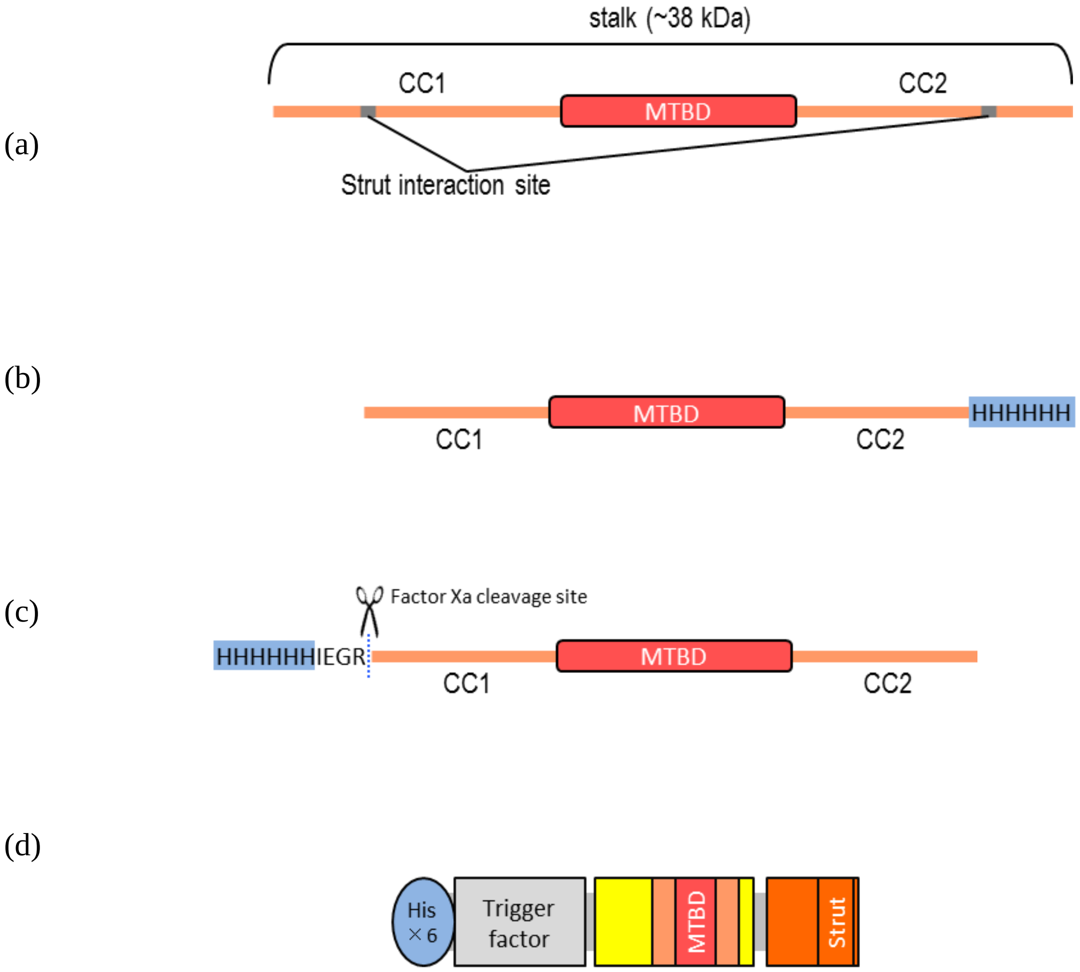

**Figure 2.1 Basic designs of constructs**

Designs of dynein constructs including stalk region were shown.

(a) Schematic view of whole stalk region

(b) mDS277-His, mDS269-His, mDS262-His, dDS278-His, DNAH7s291-His

(c) DHC8s289, DHC9s288

(d) His-TF-h4st5

**mDS277α-His**

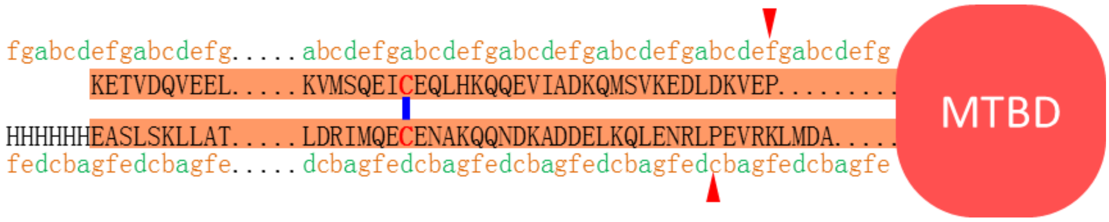

**dDS277-β-His**

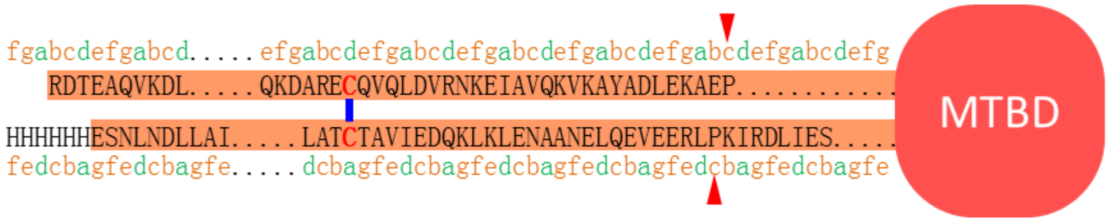

**dDS277α-His**

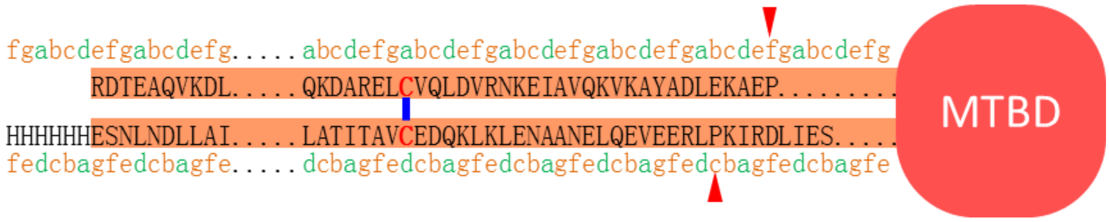

**dDS277+β-His**

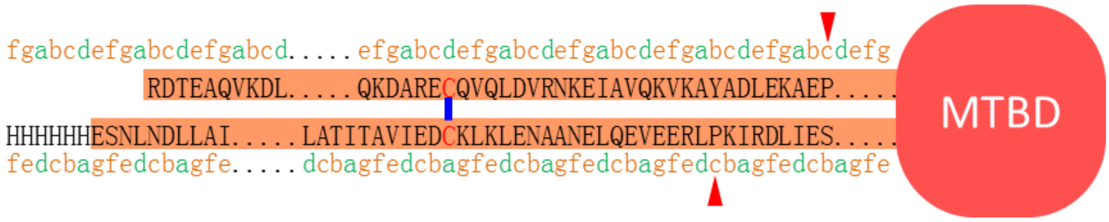

**Figure 2.2 Construct design of cysteine introduced stalk regions**

Designs of dynein stalk constructs with His-tag at the C-terminus are shown. Each registry can be fixed by S-S linkage when engineered cysteine residues colored in red are introduced.

mDS277α-His : mouse dynein stalk in an α registry. dDS277-β-His: *Dictyostelium* dynein stalk in a –β registry. dDs277α-His: *Dictyostelium* dynein stalk in an α registry. dDs277+β-His: *Dictyostelium* dynein stalk in a +β registry.

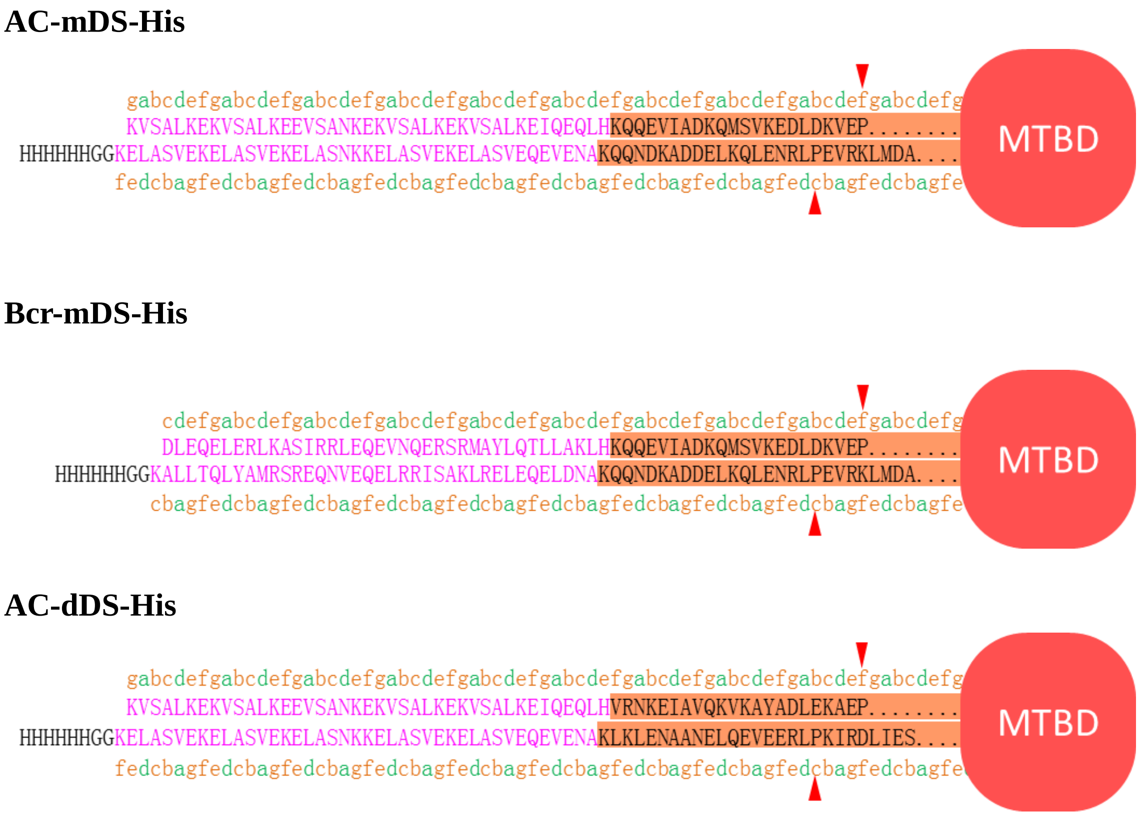

**Figure 2.3 Construct design of chimeric stalk fused with stable coiled coil**

Designs of chimeric dynein stalk constructs fused with stable coiled coil are shown. Artificial coiled coil were fused to mouse and *Dictyostelium* dynein stalk region, AC-mDS-His and AC-dDS-His. Thermophilic bacterial coild coil was fused to mouse dynein stalk, Bcr-mDS-His. Regions colored in magenta indicate the fused coiled coil structure.

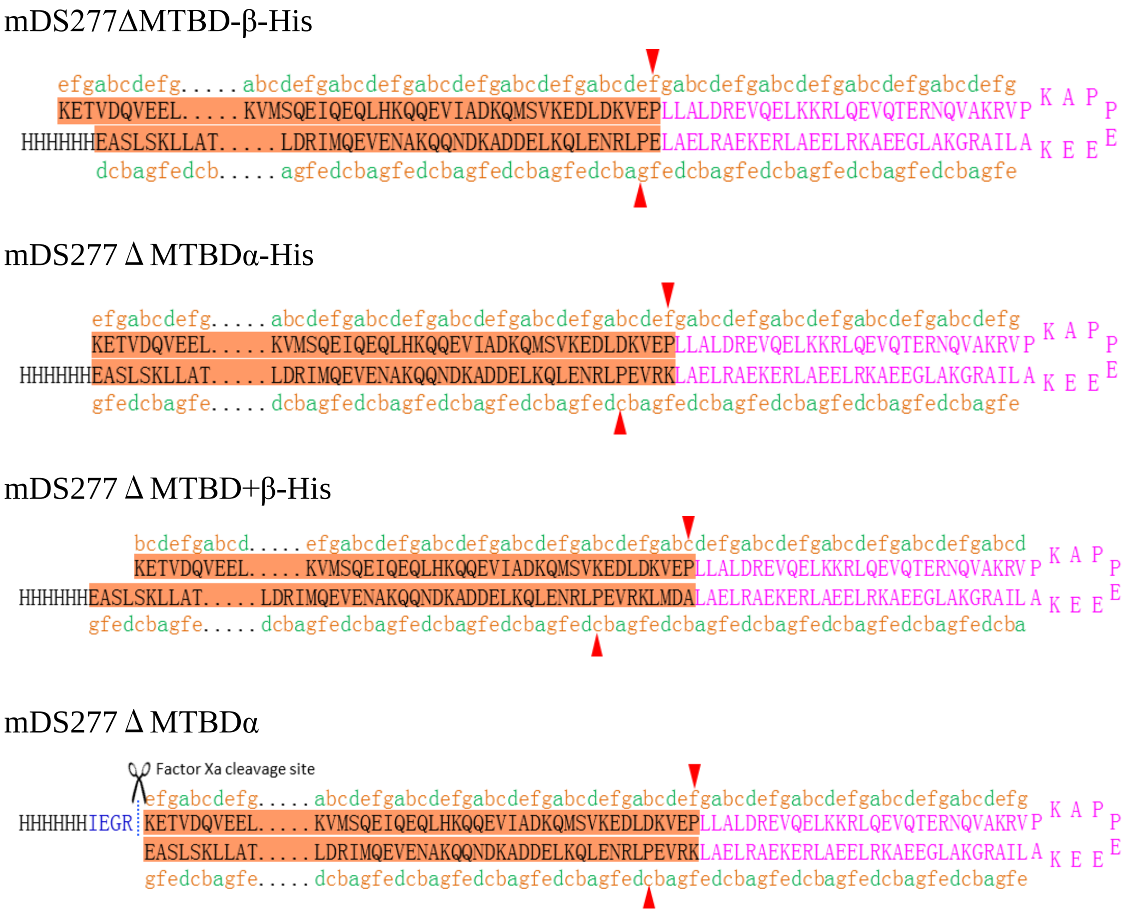

**Figure 2.4 Construct design of headless stalk**

Designs of headless dynein stalk without MTBD are shown. Basic sequence was mouse dynein stalk (mDS277). Regions colored in magenta indicate the simple coiled coil connected by a short turn of seryl-tRNA synthetase of *Thermus thermophilus* instead of MTBD [Yaremchuk *et al.*, 1992]. mDS277ΔMTBD α has a cleavage site to remove the His-tag.

## 2.2 Protein production and preparation

### 2.2.1 Production of recombinant protein

Expression vectors were introduced into *E. coli* BL21 (DE3), BL21-CodonPlus (DE3)-RIL or Rosetta2 (DE3). Conditions of cultivation and induction were optimized for each construct. In constructs of mDS262-His, DHC8s289, DHC9s288 and His-TF-h4st5, cells were grown in LB medium (1 % Trypton, 0.5 % Yeast extract, 1 % NaCl) to $OD_{600nm}$ of 0.5 at 310 K. Then, protein expression was induced by addition of 0.1 mM isopropyl β-D-1-thiogalactopyranoside (IPTG) at 289 K for 16 hours. The other constructs were grown in a kind of auto induction medium modified from Studier's method [Studier, 2005]. The protein production was induced simultaneously with the cell growth. Cells were cultivated in Lactose-LB medium (1 % Trypton, 0.5 % Yeast extract, 1 % NaCl, 0.1 % lactose, 0.5 % glycerol, 20 mM Tris-HCl pH 7.5) for 16 hours at 310 K. After induction the cells were harvested by centrifuge and frozen by liquid nitrogen. Frozen cells were stored at 193 K.

### 2.2.2 Ni-affinity chromatography

Frozen cells were resuspended by Lysis buffer (50 mM Tris-HCl pH 7.0, 400 mM NaCl, 1 mM phenylmethylsulfonyl fluoride (PMSF), 1 mM benzamidine, 1 mM 6-aminocaproic acid). Cells were lysed by two passages through a French Press (AMINCO) at 20,000 PSI. The lysate was clarified by ultracentrifugation (164,430 g, 30 min), and the supernatant was mixed with 3 mL Ni-IMAC resin (BIO-RAD) and then incubated for 30 min. The affinity resin with the bound His-tagged protein was then packed into a 20 mL volume open column. The resin was washed with 10 column volumes of wash buffer (50 mM Tris-HCl pH 7.0, 400 mM NaCl, 10 mM imidazole), then the protein was eluted with elution buffer (50 mM Tris-HCl pH 7.0, 400 mM NaCl, 300 mM imidazole).

### 2.2.1 Oxidative disulfied cross-linking

Cysteine-introduced constructs of mDS277α and dDS277α in order to lock the registry was obtained by a modified procedure of the previous report [Kon *et al*., 2009]. After His-tag purification, the protein sample was desalted by a PD10 desalting column (GE Healthcare) with gel-filtration buffer (50 mM Tris-HCl pH 7.0, 400 mM NaCl). The sample was oxidized by addition of 0.1 mM copper-phenanthroline, and then oxidation was stopped by addition of 5 mM EDTA after 30 minutes incubation on ice. Formation of intramolecular disulfide bond was confirmed by non-reducing SDS-PAGE (**Figure 2.5**).

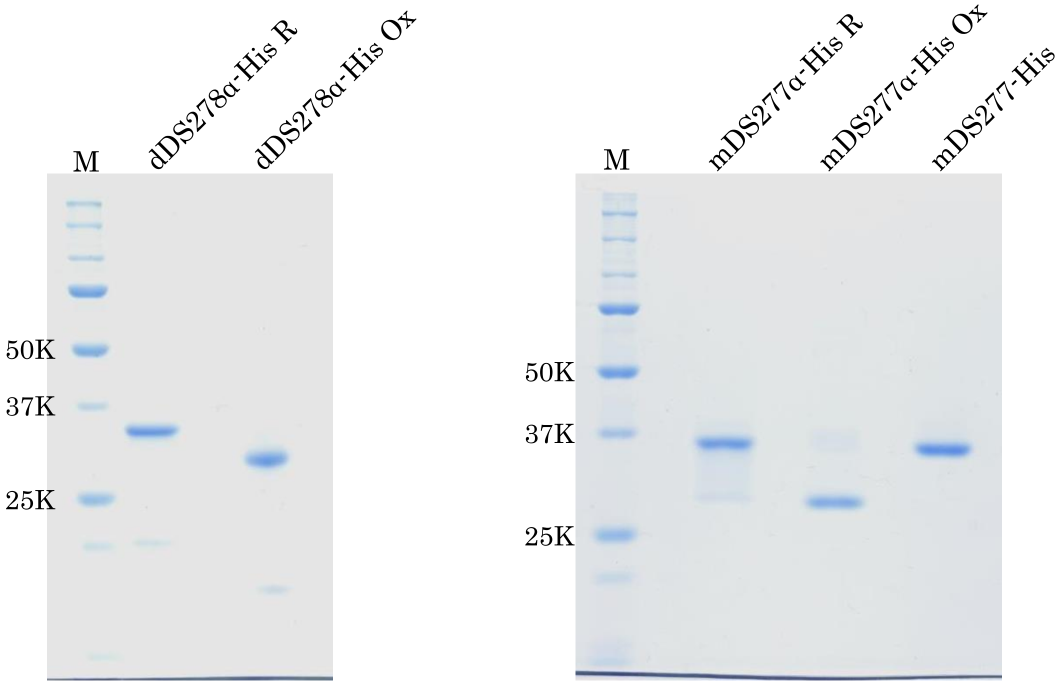

**Figure 2.5 Non-reducing SDS-PAGE of dDS277α (left) and mDS277α-His (right)**

Electrophoretic mobility shift assay of cysteine-introduced stalk fragments.

Left; Lanes are protein standard (M), dDS278α-His without cross-linkage, dDS278α-His with cross-linkage.

Right; Lanes are protein standard (M), mDS277α-His without cross-linkage, mDS277α-His with cross-linkage, and mDS277-His from left to right.

### 2.2.2 Removal of 6× His tag by Factor Xa cleavage

6× His tag of mDS277ΔMTBDα was removed by Factor Xa cleavage. His-tag purified protein was desalted by a PD10 Desalting column with cleavage buffer (50 mM Tris-HCl pH 7.0, 100 mM NaCl, 5 mM $CaCl_2$). Factor Xa (Merck) was added to about 1.2 mg/mL protein to a final concentration of 13.3 Units/mL and incubated 48 hours at 294 K. The efficiency of protein cleavage was checked by SDS-PAGE (**Figure 2.6**). Cleavage product was through Xarrest Agarose and Ni-IMAC resin for capturing Factor Xa and uncleaved His-tagged protein, respectively. The digested protein was applied to a gel filtration column as described below.

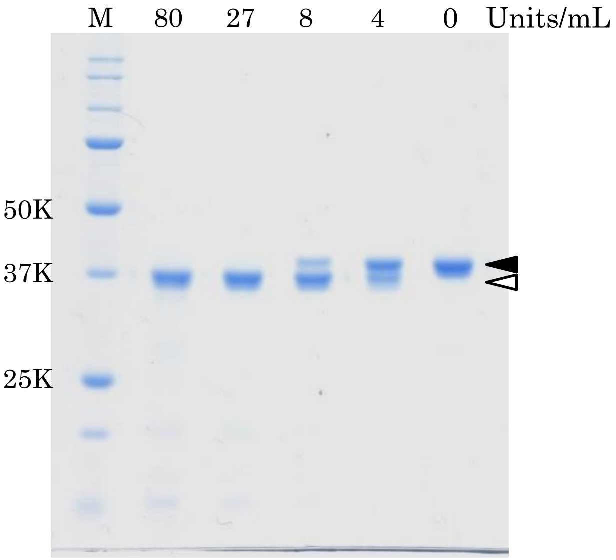

**Figure 2.6 Digestion test by Factor Xa in DHC9s288**

6× His tag was removed by protease Factor Xa. Cleavage efficiency was checked by standard SDS-PAGE. Lanes are Marker and DHC9s288 proteins incubated with 80~0 Units/mL Factor Xa at 294 K for 42 hours. The filled wedge points bands of uncleaved DHC9s288, while the open wedge points cleaved one.

### 2.2.3 Gel filtration chromatography

Finally, tag-affinity purified protein was applied to HiLoad 26/60 Superdex75 pg gel filtration column (GE Healthcare) equilibrated in gel-filtration buffer (**Figure 2.7 and Figure 2.8**). Fractions containing the purified proteins were concentrated to appropriate concentration for each structural analysis by ultrafiltration membrane (5,000 MWCO; Millipore Corporation).

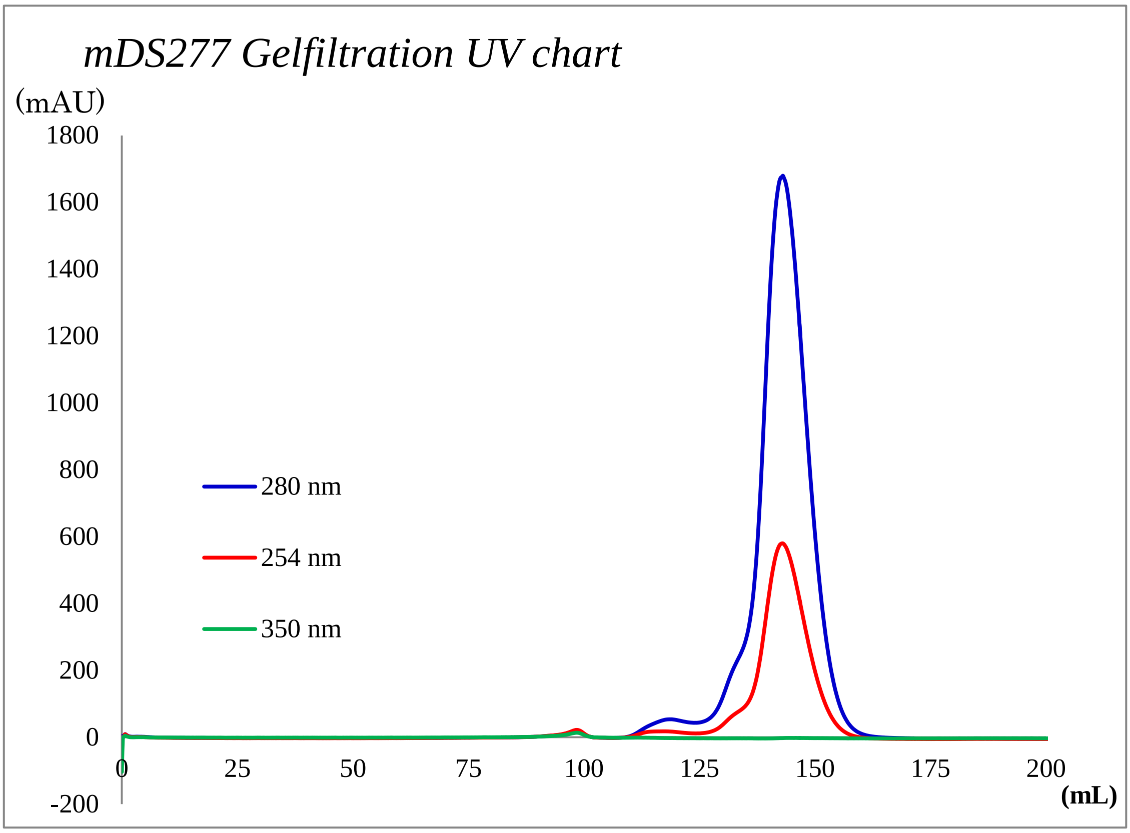

**Figure 2.7 Column chromatogram of the final gel-filtration**

The case of mDS277-His is shown here as a representative. The chromatogram chart showed a single peak in each construct.

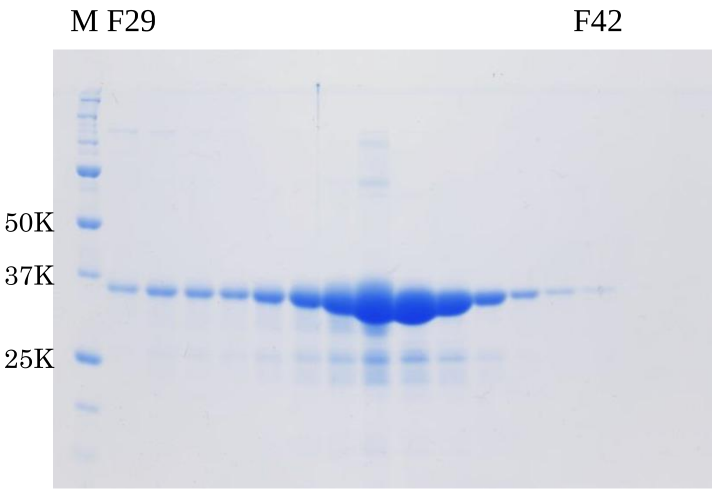

**Figure 2.8 SDS-PAGE of mDS277 after gel-filtration**

Samples from tube fractions from 29 to 42 (116 – 168 mL) were applied on the gel to check homogeneity of the sample. SDS-PAGE of mDS277 was shown as a representative of the gel.

## 2.3 Structure determination by X-ray crystallography

### 2.3.1 Screening of crystallization conditions

Crystallization conditions of the proteins were screened by hanging-drop vapor diffusion method. 2 µL crystallization drops composed of 1 µL protein solution and 1 µL reservoir solution were made on siliconized cover slide glass (HR8-090, Hampton reseach) and vapor equibrated to 150 µL reservoir solutions on 48 well plate (HR3-275, Hampton reseach) . Initial screening of crystallization conditions was carried out with several commercially available screening kits (Crystal Screen 1 and 2, Crystal Screen Lite, Crystal Screen Cryo, PEG/Ion Screen, Index 1 and 2, SaltRx 1 and 2, Grid Screen Ammonium Sulfate, NaCl, PEG 6000, and MPD, Crystal Screen Cryo, MembFac and Natrix [Hampton research], Wizard 1, 2, 3 and 4, Ozma 1K, 4K, Cryo1 and 2 and PRECIPITANT SYNERGY [Emerald BioSystems], Stura FootPrint Screens, MemSys and MemGold1 [Molecular Dimensions] and MbClass Suite [QIAGEN]) at 277 K or 293 K. As a results, protein crystals of mDS277-His, mDS277ΔMTBDα-His, mDS277ΔMTBDα and mDS277ΔMTBD+β-His were obtained (**Figure 2.9**). These initial crystallization conditions were optimized and the resultant crystals were provided to X-ray diffraction measurements. Among obtained crystals, only that of mDS277-His satisfied required quality for X-ray structural solution.

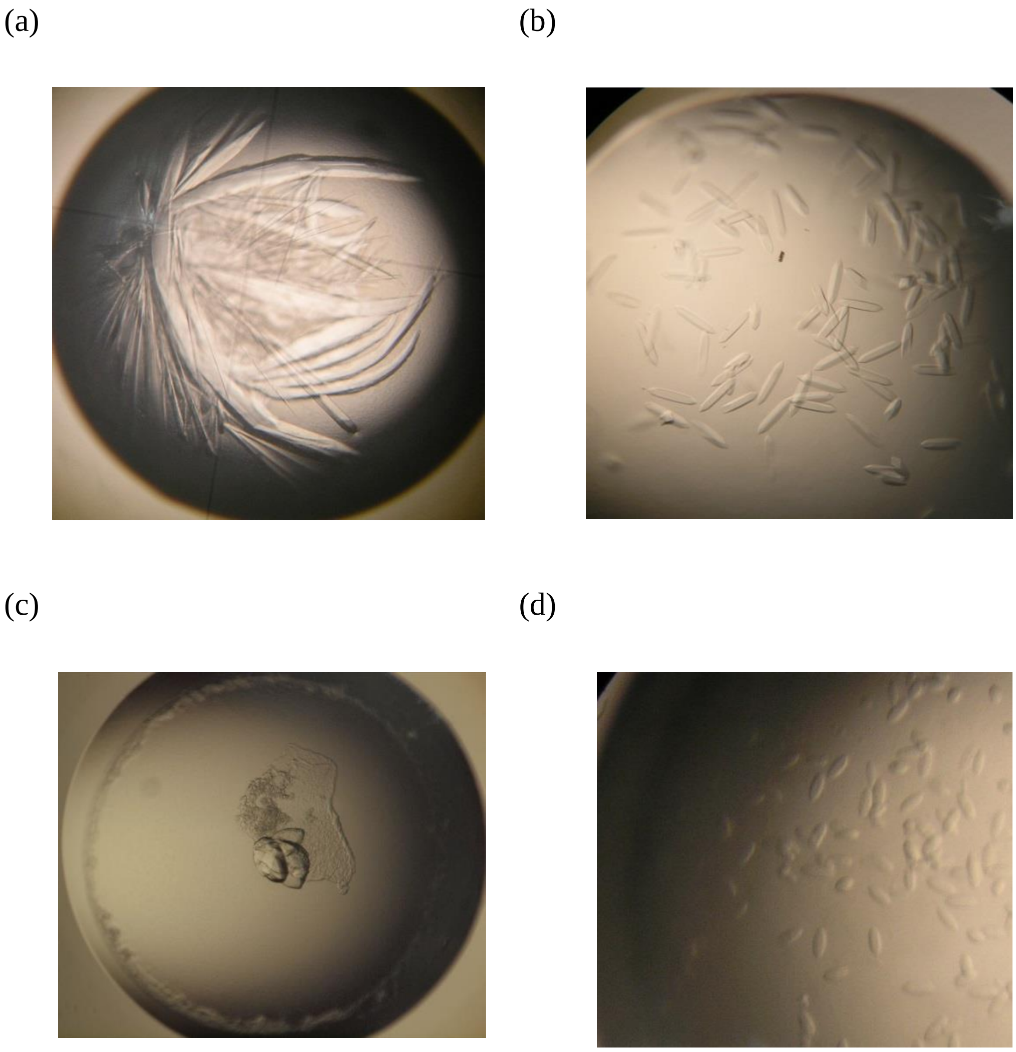

**Figure 2.9 Crystals of dynein stalk region**

Photographs of obtained crystals of (a) mDS277-His, (b) mDS277ΔMTBDα-His, (c) mDS277ΔMTBDα and (d) mDS277ΔMTBD+β-His.

### 2.3.2 Crystallization & post crystallization treatment

The mDS277-His, mDS277ΔMTBDα-His, mDS277ΔMTBDα and mDS277ΔMTBD+β-His were crystallized by hanging-drop vapor diffusion method at 277K. The 2 μL crystallization drops were vapor equilibrated to 150 μL reservoir solutions. In case of mDS277-His, crystallization drops contained 1 μL protein solution (~20 mg/mL) in gel filtration buffer and 1 μL of reservoir solution (0.20 M $NH_4H_2PO_4$, 20% PEG3350) and vapor equilibrated for 14 days. Then obtained crystals were soaked into 0.15 M $NH_4H_2PO_4$, 20 % PEG3350, 10% glycerol and incubated at 277 K. 24 hours later, the crystals were flash-cooled and stored in liquid nitrogen.

In case of mDS277ΔMTBDα-His, the drops contained 1 μL (~30 mg/mL) of the protein and 1 μL of reservoir solution (0.10 M $CH_3COONa$ pH 4.6, 28% 2-Methyl-2,4-pentanediol [MPD]) and vapor equilibrated for about 10 days. Then obtained crystals were soaked into 0.07 M $CH_3COONa$ pH 4.6, 20% MPD, 15 mM Tris-HCl pH 7.0, 0.12 M NaCl. Soaked crystals were immediately flash-cooled and stored in liquid nitrogen.

In case of mDS277ΔMTBDα, the drops contained 1 μL (~30 mg/mL) of the protein and 1 μL of reservoir solution (0.10 M Sodium citrate pH 5.5, 35% 2-propanol, 5 % PEG1000) and vapor equilibrated for about 1 month. Then obtained crystals were harvested from crystallization drops and flash-cooled directly by liquid nitrogen.

In case of mDS277ΔMTBD+β-His, the droplets contained 1 μL (~20 mg/mL) of the protein and 1 μL of reservoir solution (0.1 M $CH_3COONa$ pH 4.5, 30% PEG200, 0.10 M NaCl) and vapor equilibrated for about 1 month. Then obtained crystals were picked up from crystallization drops and flash-cooled by liquid nitrogen.

### 2.3.3 X-ray data collection

X-ray diffraction images were collected at 100K. All data sets were collected at the synchrotron beamlines; BL-17A, Photon Factory or BL44XU, SPring-8.

Crystals of mDS277ΔMTBD+β-His were diffracted to ~8 Å resolution (**Figure 2.10**). The complete data set was not collected because of the low resolution of the X-ray diffraction.

Crystals of mDS277ΔMTBDα-His diffracted to ~7 Å resolution (**Figure 2.11a** and **Table 2.1)**. Molecular replacement using the previously reported SRS-MTBD structure (PDB ID: 3ERR) as a search model was tested to obtain the initial phase angles, however it failed and no possible solutions were found.

To improve the resolution limit of the mDS277ΔMTBDα-His crystals, mDS277ΔMTBDα, the protein sample without the His×6 tag, was crystallized with 27.5% 2-Propanol, 5% PEG1000 and 0.1 M Sodium citrate pH 6.0. Difference between mDS277ΔMTBDα-His and mDS277ΔMTBDα was only presence of His×6 tag but the crystallization conditions and properties of crystals were completely changed. The diffraction limit of ΔMTBDα reached ~2.5 Å (**Figure 2.11b** and **Table 2.1)**. However, like the case of mDS277ΔMTBDα-His, molecular replacement did not find possible solutions for the data set of mDS277ΔMTBDα.

Crystals of mDS277-His were diffracted to 3.5 Å resolution with glycerol treatment after crystallization (**Figure 2.12a** and **Table 2.2**). Interestingly, crystals treated with 35% PEG3350 were dehydrated and diffracted up to 2.5 Å. Dehydrated crystals looks better than those treated with glycerol in terms of resolution limit (**Figure 2.12b** and **Table 2.2**).

As described above, treatment with 35% PEG3350 dramatically improved the diffraction qualities of mDS277-His crystals. Changes of cell dimensions and space group were observed between these two types of crystals. It is considered that the crystal dehydration induced these changes.

At first, I tried to obtain phase information by molecular replacement using data set of 2.5 Å resolution from dehydrated crystals and that of 3.5 Å resolution from glycerol treated one with the dynein MTBD structure (PDB ID: 3ERR) as a search model. However, despite the perfect amino acid sequence identity of the MTBD region, I was unable to obtain satisfactory solutions from the molecular-replacement calculations. Secondly phase determinations by the single-wavelength anomalous dispersion method (SAD) with Seleno-L-Methionine (SeMet) derivatives were tried. Only the data set of 4.0 Å resolution from a glycerol treated crystal provided an interpretable electron density map for model building.

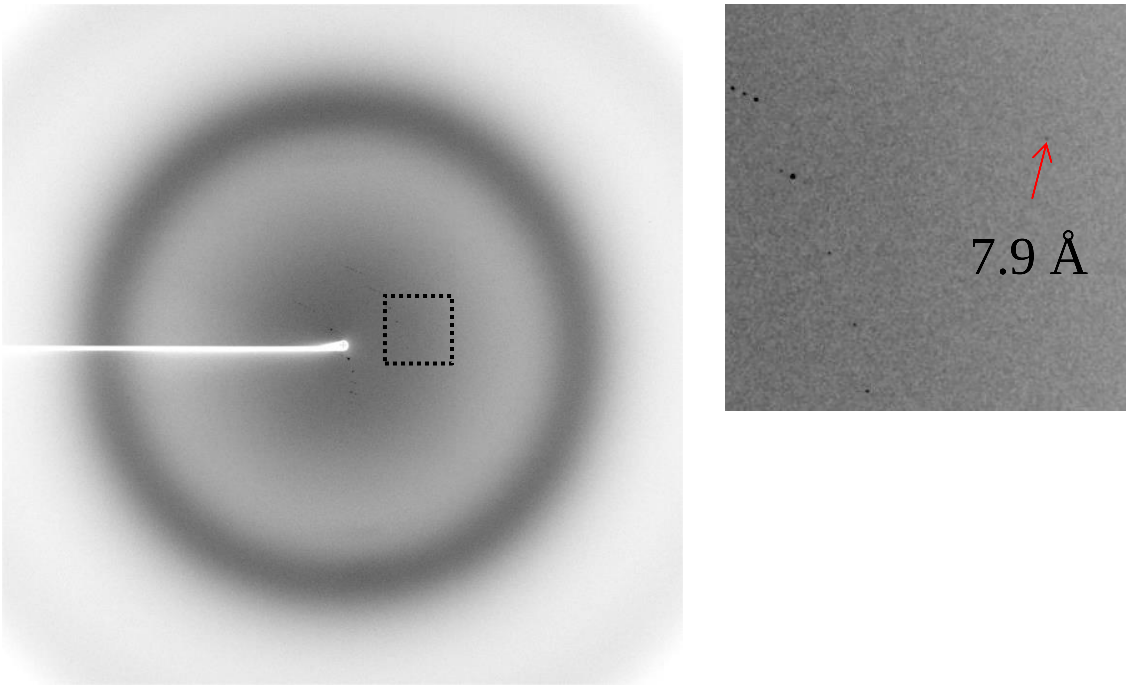

**Figure 2.10 X-ray diffraction pattern from the mDS277ΔMTBD +β crystal. Small panel shows a close up view of the pattern.**

The X-ray diffraction pattern of the crystal of mDS277ΔMTBD+β collected at the synchrotron beamline BL44XU in SPring-8 is shown.

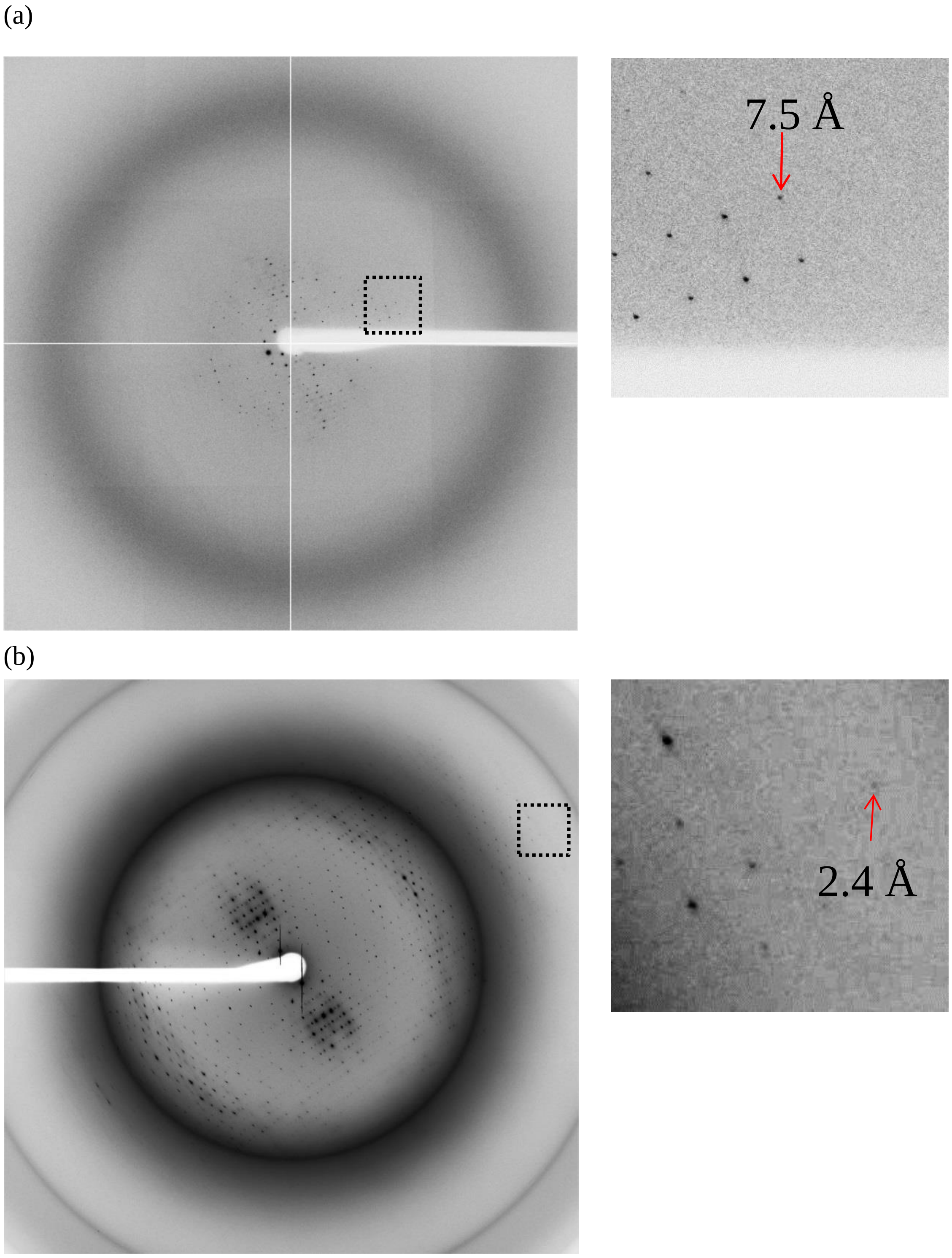

**Figure 2.11 X-ray diffraction pattern from mDS277ΔMTBD crystals. Small panel shows a close up view of the pattern.**

(a) Diffraction pattern from a crystal of mDS277ΔMTBDα-His.

(b) Diffraction pattern from a crystal of mDS277ΔMTBDα.

**Table 2.1 Crystallographic statistics of mDS277ΔMTBD crystals**

| | **mDS277ΔMTBDα** | **mDS277ΔMTBDα-N-His** |
|---|---|---|
| X-ray Source | BL-17A | BL44XU |
| Space group | $I422$ or $I4_122$ | $C2$ |
| Unit-cell parameters | | |
| $a$ (Å) | 140.24 | 186.70 |
| $b$ (Å) | 140.24 | 71.12 |
| $c$ (Å) | 291.49 | 109.72 |
| $\alpha$ (°) | 90 | 90 |
| $\beta$ (°) | 90 | 123.00 |
| $\gamma$ (°) | 90 | 90 |
| Wavelength (Å) | 1.00000 | 0.90000 |
| Detector | Quantum 210 | MX-225-HE |
| Detector distance (mm) | 300 | 300 |
| Oscillation angle (°) | 1.0 | 1.0 |
| Oscillation range (°) | 180 | 180 |
| Resolution range (Å) | 50.00-7.40(7.53-7.40) | 50.00-3.40(3.46-3.40) |
| Exposure time / image (s) | 5.0 | 1.0 |
| Total reflections | 27,131 | 58,945 |
| Unique reflections | 2,138 | 16,971 |
| Completeness (%) | 99.7(100) | 98.3(100) |
| $R_{\mathrm{merge}}(I)$ (%)[a] | 6.9(86.0) | 6.5(45.5) |
| $< I/\sigma(I) >$ | 41.4(2.8) | 20.7(2.2) |

Values in parentheses are for the highest resolution shells.

[a] $R_{\mathrm{merge}}(I) = \Sigma_{hkl}\Sigma_i |I_i (hkl) - <I (hkl)>| / \Sigma_{hkl}\Sigma_i I_i (hkl)$, where $I_i (hkl)$ is the value of the $i$ th measurement of the intensity of reflection $hkl$, $<I (hkl)>$ is the mean value of the intensity of the reflection $hkl$ and the summation is the overall measurement.

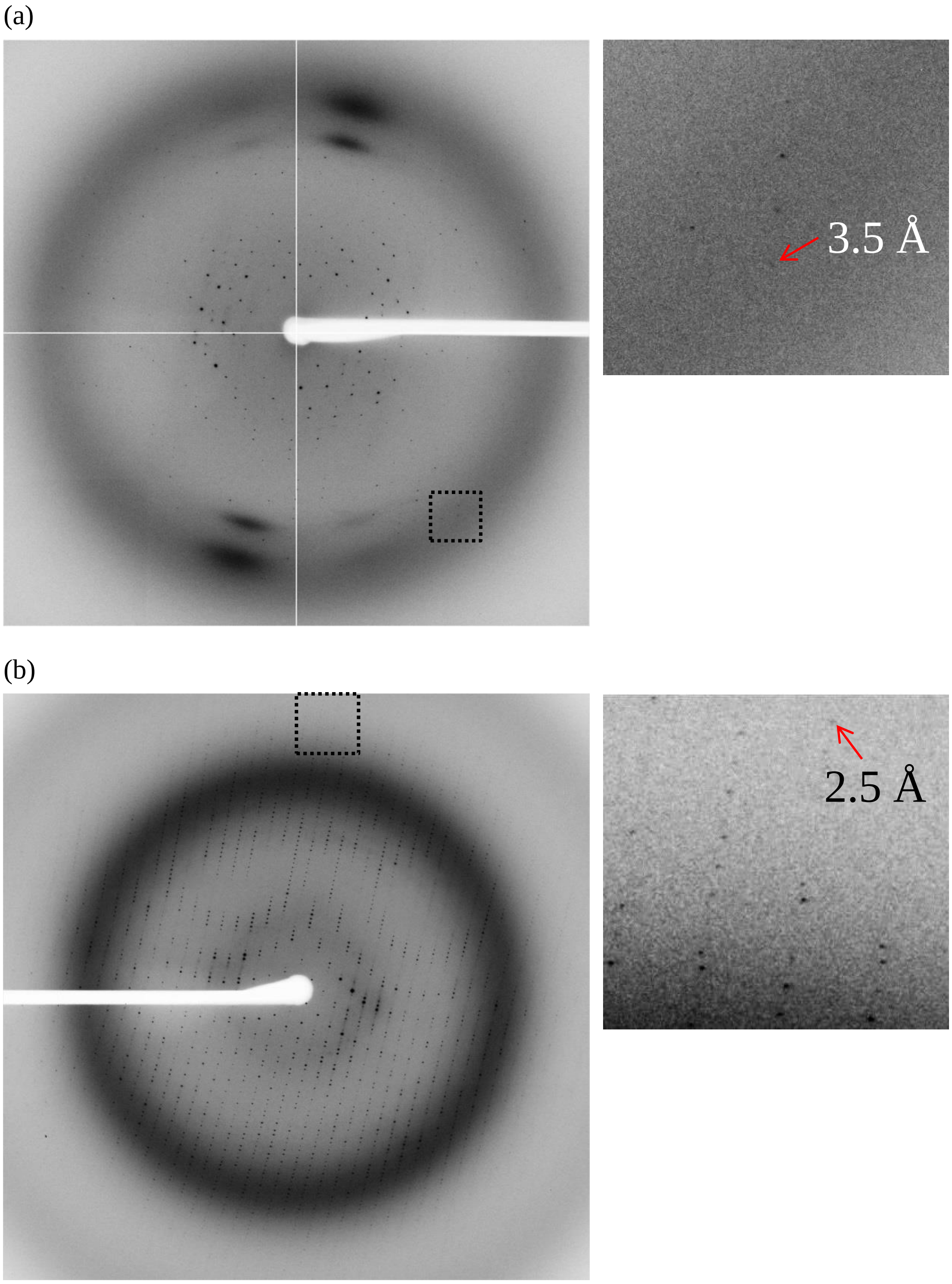

**Figure 2.12 X-ray diffraction pattern from mDS277-His crystals. Small panel shows a close up view of the pattern.**

(a) Diffraction pattern from a crystal of mDS277-His.

(b) Diffraction pattern from a crystal of mDS277-His dehydrated.

**Table. 2.2 Crystallographic statistics of mDS277-His crystals**

| | **mDS277-His Native** | **mDS277-His (SeMet-Peak)** | **mDS277 -His Dehydrated** |
|---|---|---|---|
| X-ray Source | BL-17A | BL44XU | BL44XU |
| Space group | $P3_121$ | $P3_121$ | $P3_112$ or $P3_212$ |
| Unit-cell parameters | | | |
| $a$ (Å) | 102.94 | 103.57 | 181.98 |
| $b$ (Å) | 102.94 | 103.57 | 181.98 |
| $c$ (Å) | 69.07 | 69.69 | 49.46 |
| $\alpha$ (°) | 90 | 90 | 90 |
| $\beta$ (°) | 90 | 90 | 90 |
| $\gamma$ (°) | 120 | 120 | 120 |
| Wavelength (Å) | 1.00000 | 0.97917 | 0.90000 |
| Detector | Quantum 210 | MX-225-HE | MX-225-HE |
| Detector distance (mm) | 300 | 450 | 295 |
| Oscillation angle (°) | 1.0 | 1.0 | 1.0 |
| Oscillation range (°) | 100 | 180 | 94 |
| Resolution range (Å) | 50.00-3.50(3.56-3.50) | 50.00-4.00(4.07-4.00) | 50.00-2.50(2.54-2.50) |
| Exposure time / image (s) | 15.0 | 1.5 | 4.0 |
| Total reflections | 33,235 | 41,411 | 177,401 |
| Unique reflections | 5,560 | 3,846 | 32,434 |
| Completeness (%) | 99.9(100) | 99.9(100) | 99.6(99.2) |
| $R_{\text{merge}}(I)$ (%)[a] | 7.8(59.8) | 9.3(73.3) | 6.5(45.3) |
| $< I/\sigma(I) >$ | 29.2(3.3) | 39.7(5.0) | 37.5(4.4) |
| No. of sites | - | 12 | |
| FOM | - | 0.42 | |

Values in parentheses are for the highest resolution shells.

[a] $R_{\text{merge}}(I) = \Sigma_{hkl}\Sigma_i |I_i(hkl) - \langle I(hkl)\rangle| / \Sigma_{hkl}\Sigma_i I_i(hkl)$, where $I_i(hkl)$ is the value of the $i$ th measurement of the intensity of reflection $hkl$, $\langle I(hkl)\rangle$ is the mean value of the intensity of the reflection $hkl$ and the summation is the overall measurement.

### 2.3.4 Structure determination of mDS277

All diffraction images were processed by HKL-2000 software [Otwinowski *et al.*, 1997]. Structure solution and refinement were performed by Phenix software suite [Adams *et al.*, 2002]. The phase angles were initially determined from 4.0 Å resolution dataset using the SAD method. The interpretable electron density map to build the structural model was provided by the SAD calculation with Phenix AutoSol [Terwilliger *et al.*, 2009]. The SAD calculation has confirmed that the protein was packed into a space group of $P3_121$ with one molecule per asymmetric unit. The Matthews coefficient ($V_M$) of the crystal was estimated as 3.25 $Å^3$ $Da^{-1}$ and its solvent content was 62% [Matthews, 1968]. The SeMet derivative includes twelve Se atoms per one polypeptide, and the positions of eight Se atoms were detected in the anomalous difference Fourier map (**Figure 2.13)**. The model was built using COOT software [Emsley *et al.*, 2010] along with the experimental electron density map. We fitted the MTBD structure [Carter *et al.*, 2008, PDB ID: 3ERR] to the electron density map and extended the N-terminal and C-terminal helices from the fitted MTBD. Phenix.refine was used for model refinement of the native structure at 3.5 Å resolution [Afonine *et al.*, 2012]. The model included a portion of the polypeptide from Thr3209 to Asn3471 (262 of 277 residues) and was refined to the values of $R_{work}$=0.27 and $R_{free}$=0.30. The final structure was validated using MOLPROBITY [Lovell *et al.*, 2003]. The analysis showed that 89.7% of the residues were in Ramachandran favored, with no residues as outliers. The final statistics of crystallographic refinement are shown in **Table 2.3.**

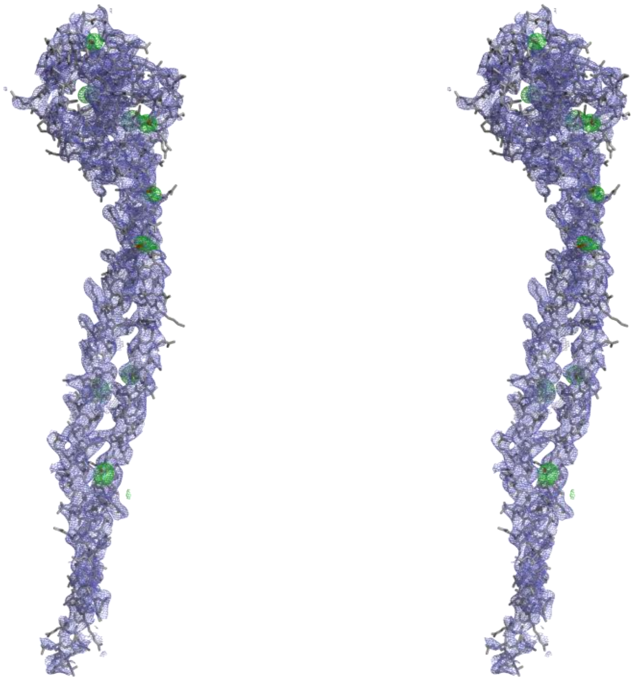

**Figure 2.13 Stereo view of the electron density map of mDS277-His**

The electron density map of mDS277-His at 3.5 Å resolution is depicted in a wall-eye stereo view. The 2*mF*o-*DF*c map in purple was contoured at a 1.0 $\sigma$ cutoff on the model of mDS277-His [Read, 1986]. Green densities depict the anomalous map contoured at a 6.0 $\sigma$ cutoff.

**Table 2.3 Crystallographic statistics of the final model**

| ***Refinement statistics*** | |
|---|---|
| Resolution | 44.57-3.50 |
| $R_{\text{work}}$ (%)[b] / $R_{\text{free}}$ (%)[c] | 27.88/30.49 |
| No. of atoms | |
| Protein | 1962 |
| Ligand/ion | 0 |
| Water | 0 |
| Overall mean $B$ factor (Å$^2$) | 172.2 |
| RMSD from ideal values | |
| Bond length (Å) | 0.005 |
| Bond angles (°) | 1.18 |
| Ramachandran plot | |
| Favored regions (%) | 90 |
| Allowed regions (%) | 10 |
| Disallowed regions (%) | 0 |

[b] $R$-factor$=\Sigma \mid |F_{obs}(hkl)| - |F_{calc}(hkl)| \mid / \Sigma \mid F_{obs}(hkl) \mid$.

[c] $R_{\text{free}}$ is the $R$-factor computed for the test set of reflections that were omitted from the refinement process

## 2.4 CD spectrum

Far-UV CD spectra measurement was carried out on a J-820 spectropolarimeter (JASCO Co.) at 25 °C under constant nitrogen flux. Spectra were recorded in 0.1 cm quartz cells from 195 to 250 nm using the continuous-scan option (100 nm/min), with a step size of 0.5 nm, response time of 1 sec and a bandwidth of 1 nm. The protein solutions used for the CD measurements contained 5 mM Tris-HCl pH 7.0, 50 mM NaCl with or without 1 mM dithiothreitol (DTT) at a concentration of 0.1~0.2 mg/mL. The results were expressed as mean residue ellipticity [$\Theta$] deg cm$^2$ dmol$^{-1}$ (**Figure 2.14**). Molecular ellipticity values at 222 nm were used to calculate the relative helix content [Chen *et al*., 1971].

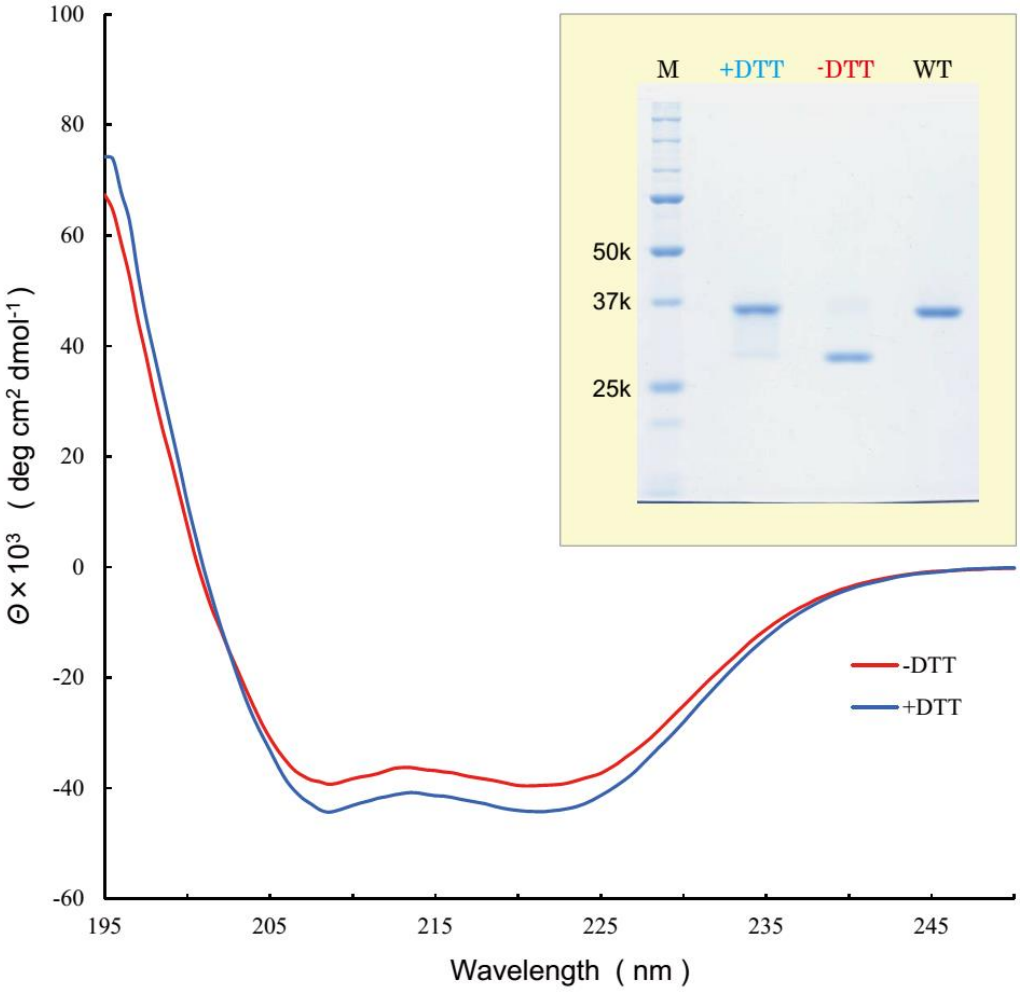

**Figure 2.14 Secondary structure analysis of the entire stalk region with two different registries**.

Far UV CD spectra of cysteine-introduced mDS277-His with (red) and without (blue) cross-linkage. Both spectrum exhibit α-helical characters of mDS277-His, while the spectrum of cysteine-introduced mDS277-His without cross-linkage was almost identical to that of wild-type (data not shown). Helical content of cysteine-introduced mDS277-His with cross-linkage was 11% smaller than that of the others estimated by the value of $[\Theta]_{222\mathrm{nm}}$. **Inset.** Electrophoretic mobility shift assay of cysteine-introduced mDS277-His as same as in the right panel of Figure 2.5 was shown as reference.

## 2.5 Molecular Dynamics simulations of mDS277

I executed two MD simulations of mDS277-His (wild type) and its virtual alanine double mutant. The computation system used for calculation of wild type was generated as follows: First, the N- and C-termini were protected by acetyl and N-methyl groups, respectively. Next, the protein was immersed in a 177 Å × 64 Å × 71 Å water box. Sodium and chloride ions were added to adjust the solution to physiological ionic strength (150 mM NaCl). The final system comprised 77901 atoms (4270 protein atoms, 24513 water molecules, 48 sodium ions, and 44 chloride ions). The force-field parameters for the protein, water, and ions were derived from the AMBER-based hybrid force field [Kamiya *et al.*, 2005], the flexible TIP3P water model, [Jorgensen *et al.*, 1983] and alkali and halide monovalent ion parameters [Joung *et al.*, 2008], respectively.

A virtual model of the alanine double mutant protein, P3285A/P3409A, was constructed according to the structure of the wild type using the “simple mutate” tool in COOT that replaces a corresponding residue with another. The computation system of the double mutant was prepared using the same procedure as that for the wild type. The final system comprised 77893 atoms (4262 protein atoms, 24513 water molecules, 48 sodium ions, and 44 chloride ions).

Cosgene software [Fukunishi *et al.*, 2003] was used to perform energy minimization calculations as well as an equilibration MD simulation for the wild type and the alanine double mutant protein. The conjugated gradient minimization with positional restraints on the solute using a force constant of 10 kcal/mol $Å^2$ was followed by minimization without restraint. The system was equilibrated for 100 ps using Berendsen’s NPT algorithm [Berendsen *et al.*, 1984] at 300 K, 1 bar, and a 0.5 fs time step. Electrostatic interaction was treated using the particle mesh Ewald (PME) method [Essmann *et al.*, 1995] under the periodic boundary condition. The real part cutoff distance and the dumping factor $\alpha$ were 12 Å and 0.35 $Å^{-1}$, respectively.

Psygene-G software [Mashimo *et al.*, 2013], which utilizes general-purpose computing on graphics processing units to accelerate non-bond calculations, was used for generating MD simulations. For each system, a 50-ns canonical (constant NVT) MD run was performed with box sizes of 172.2 × 62.4 × 70.5 $Å^3$ for the wild type and 176.5 × 63.4 × 67.7 $Å^3$ for the double alanine mutant at 300 K with a 1 fs time step. The SHAKE method [Ryckaert *et al.*, 1977] was applied to constrain covalent bonds between heavy atoms and hydrogen atoms. Electrostatic interaction was treated using the zero-dipole summation method [Fukuda *et al.*, 2011]. The cutoff distance and dumping factor α were 12 Å and 0.00 $Å^{-1}$, respectively. The accuracy of the zero-dipole summation method depends on α. We generated structures and dynamic properties similar to those using the PME method in a pure TIP3P water system [Fukuda *et al.*, 2012], a membrane protein system [Kamiya *et al.*, 2013], and a DNA-water-ion system [Arakawa *et al.*, 2013] when α is zero. The MD snapshot was stored at every 10 ps.

To compare the motion between the wild type and the alanine double mutant, principal component analysis was applied to each MD trajectory as follows: First, the non-hydrogen backbone atoms (n = 1056) were chosen from each trajectory, where n is number of atoms. Second, all of the MD snapshots for each trajectory were superimposed on each initial MD structure to generate $\boldsymbol{q}$, where every structure was represented by a vector as $\boldsymbol{q} = [x_1, y_1, z_1, \ldots, x_n, y_n, z_n] = [q_1, q_2, q_3, \ldots, q_{3n}]$, and *x*, *y*, and *z* are the Cartesian coordinates of the atoms. Next, the variance-covariance matrix *C* (size = 3*n* × 3*n*) was calculated. The (*i*, *j*)th element is given by $C_{ij} = \langle q_i q_j \rangle - \langle q_i \rangle \langle q_j \rangle$, where < > represents the average over each trajectory. By diagonalizing the matrix, a set of eigenvectors $\boldsymbol{\mu}_i$ and eigenvalues $\lambda i$ were obtained. Finally, the *i*th principal component $c_i$ was obtained from the equation: $c_i = \boldsymbol{\mu}_i \bullet (\boldsymbol{q} - \langle \boldsymbol{q} \rangle)$, where $\langle \boldsymbol{q} \rangle$ is the average coordinate over each trajectory. The contribution ratios of the *i*th principal component (= $\lambda_i / \Sigma\lambda_i$) for the wild type were 48.3% (*i* = 1), 24.4% (*i* = 2), 8.6% (*i* = 3), 5.1% (*i* = 4), 2.4% (*i* = 5), and for the alanine double mutant protein were 49.1% (*i* = 1), 29.5% (*i* = 2), 5.7% (*i* = 3), 4.7% (*i* = 4), and 1.8% (*i* = 5). The larger the eigenvalue, the wider the conformational space assigned to the motion. The direction of eigenvectors corresponds to that of the motion. The arrows shown in **Figure 3.12** (Chapter 3) correspond to the eigenvector of the first principal component $\boldsymbol{\mu}_1$.

From the result of MD simulations, the RMSD values of non-hydrogen main chain atoms of mDS277-His and the alanine double mutant were stabilized from 2 Å to 11 Å after 40 ps (**Figure 2.15**).

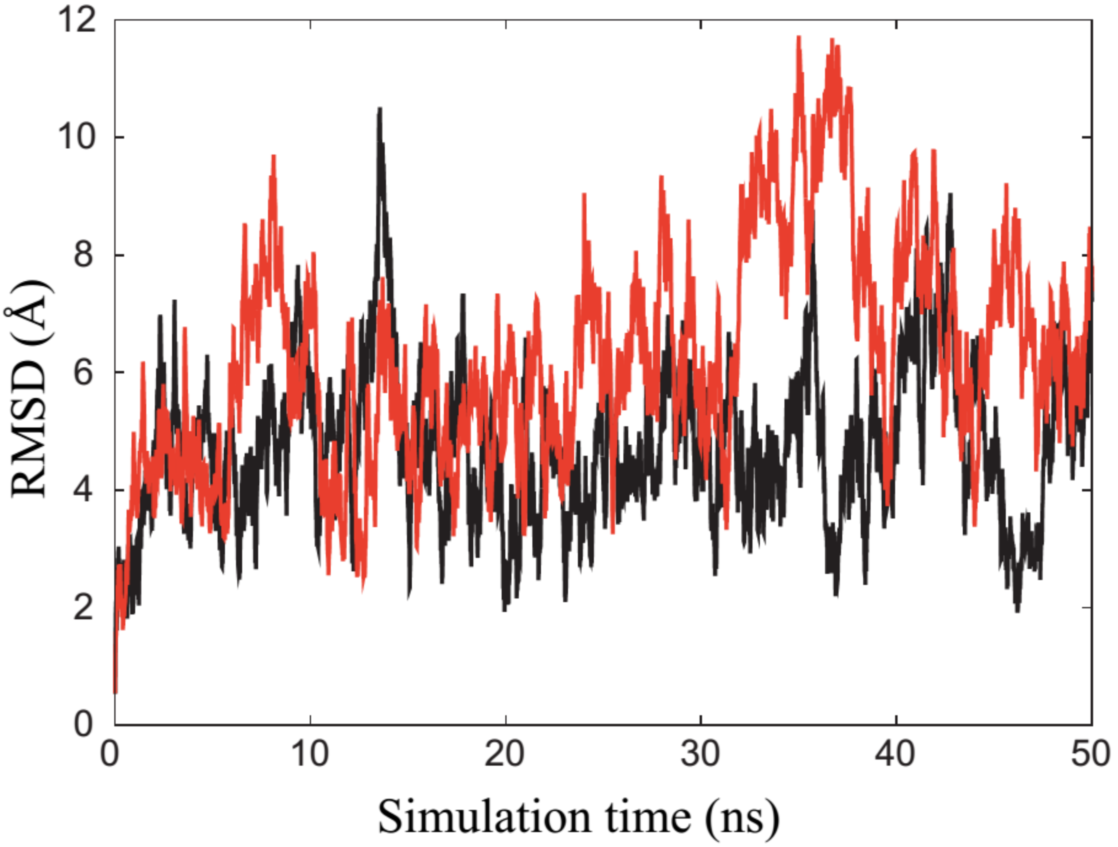

**Figure 2.15 RMSDs of backbone heavy atoms during MD simulations.**

RMSDs of the wild type (mDS277-His) and the alanine double mutant are shown by black and red lines, respectively. The reference structures for the wild type and the alanine double mutant are X-ray and modeled structures, respectively.

## 2.6 Microtubule binding assay

The binding affinity of stalk to microtubule was measured by co-sedimentation assay according to the previous report [Gibbons *et al*., 2005]. Microtubules were prepared by polymerization of purified porcine tubulin [Castoldi *et al*., 2003]. Then the microtubules were precipitated by ultra-centrifuge and resuspended in Co-sedimentation buffer (50 mM Tris-HCl pH 8.0, 50 mM $CH_3COOK$, 2 mM $MgCl_2$, 1 mM ethylene glycol tetraacetic acid, 10% glycerol, 40 µM paclitaxel). Dynein stalk was mixed with microtubule, with concentration equal to 5 µM tubulin dimer, and incubated 15 min at 300 K in Co-sedimentation buffer. After centrifugation for 15 min at 20,000 × *g*, the supernatants and resuspended precipitations were analyzed by electrophoresis and densitometric method. The SDS-PAGE gels were stained with Coomassie Brilliant Blue and converted to digital images by PC-connected scanner. The ratios of bound and unbound dynein stalk were evaluated from the band intensities of the scanned gel images. Dissociation constant of each construct were calculated by fitting a hyperbola to a plot of binding concentrations as a function of unbound stalk concentrations.

# Chapter 3

## 3. Structure and Function of the dynein stalk region

### 3.1 Microtubule binding activity of dynein stalk

Microtubule binding activity of each construct was checked by co-sedimentation assay with microtubule. Stalk constructs locked in α registry exhibited high affinity to microtubule ($K_d < 3$ μM) and this result agrees with the previous report that SRS-fusion proteins locked in α registry showed high affinity states **(Figure 3.1** and **Table 3.1**). On the other hand, mDS277-His did not show saturation phase within the experimental conditions. So, the stalk fragments without locking their registries should be fallen into +β or -β registry. The structure of mDS277 determined in this study showed the state of +β registry in fact.

The results of co-sedimentation assays with relatively big construct AAA4-Stalk-AAA5 (His-TF-h4st5) provide additional information for intramolecular communications. Nucleotide binding site on AAA4 is the nearest from MTBD among four binding sites (AAA1, AAA2, AAA3 and AAA4). In spite of the short distance between AAA4 and MTBD, the nucleotide binding state of His-TF-h4st5 has no significant effect on microtubule-binding activities (**Figure 3.2** and **Table 3.2**). Effects of P-loop mutations on *Dictyostelium* dynein motor domains were reported in 2004 [Kon *et al*., 2004]. According to the report of mutants on *Dictyostelium* dynein motor domains, the effect to motile activity by the mutation on AAA4 was not remarkable, so the result of co-sedimentation assay of His-TF-h4st5 isn’t against to the report in 2004. It could be presumed that nucleotide binding state on AAA4 has no active effect on microtubule binding activity of the dynein motor domain.

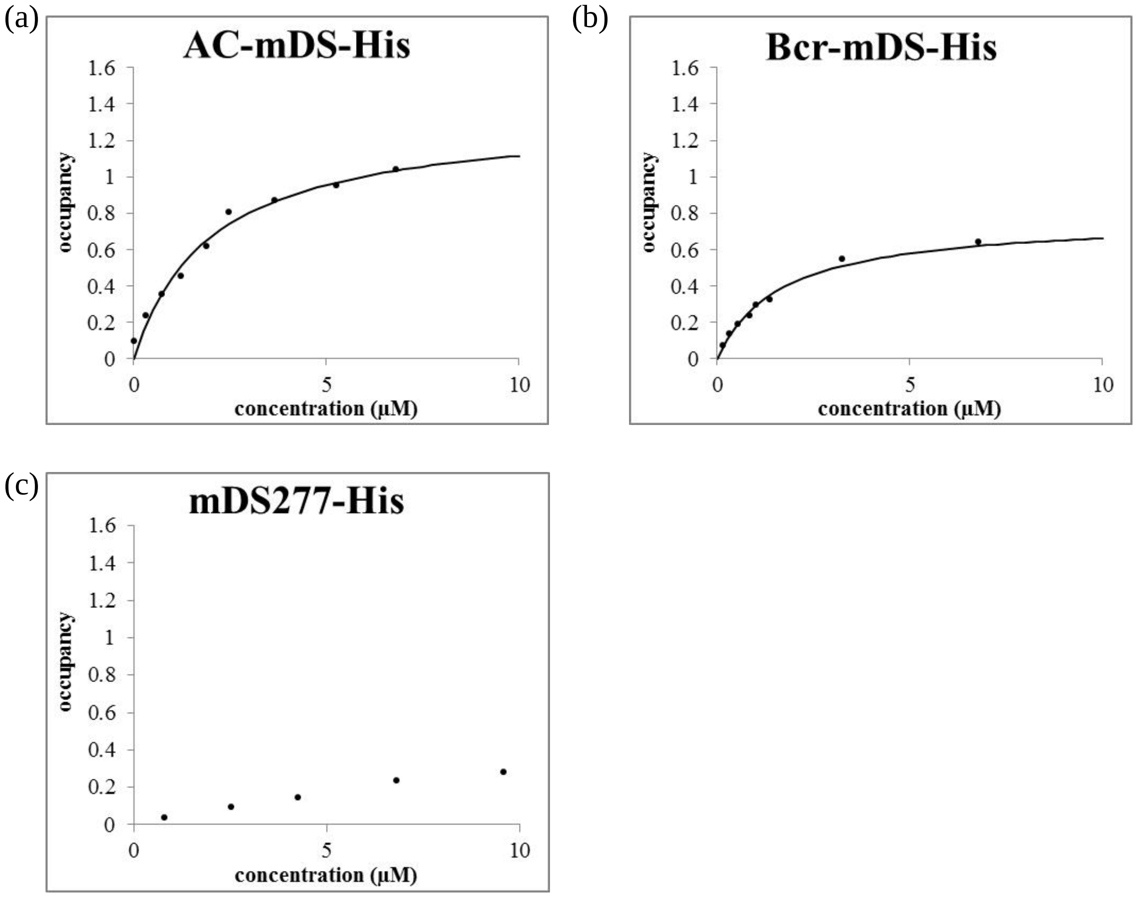

**Figure 3.1 Microtuble binding assay of mDS constructs**

(a) AC-mDS-His, (b) Bcr-mDS-His and (c) mDS277-His

**Table 3.1 Microtuble binding affinity of mDS constructs**

| construct | $K_d$ (μM) | occupancy | $R^2$ |
|---|---|---|---|
| mDS277-His | — | — | — |
| AC-mDS-His | 2.0 ± 0.35 | 1.3 ± 0.09 | 0.9803 |
| Bcr-mDS-His | 1.7 ± 0.17 | 0.77 ± 0.028 | 0.9885 |

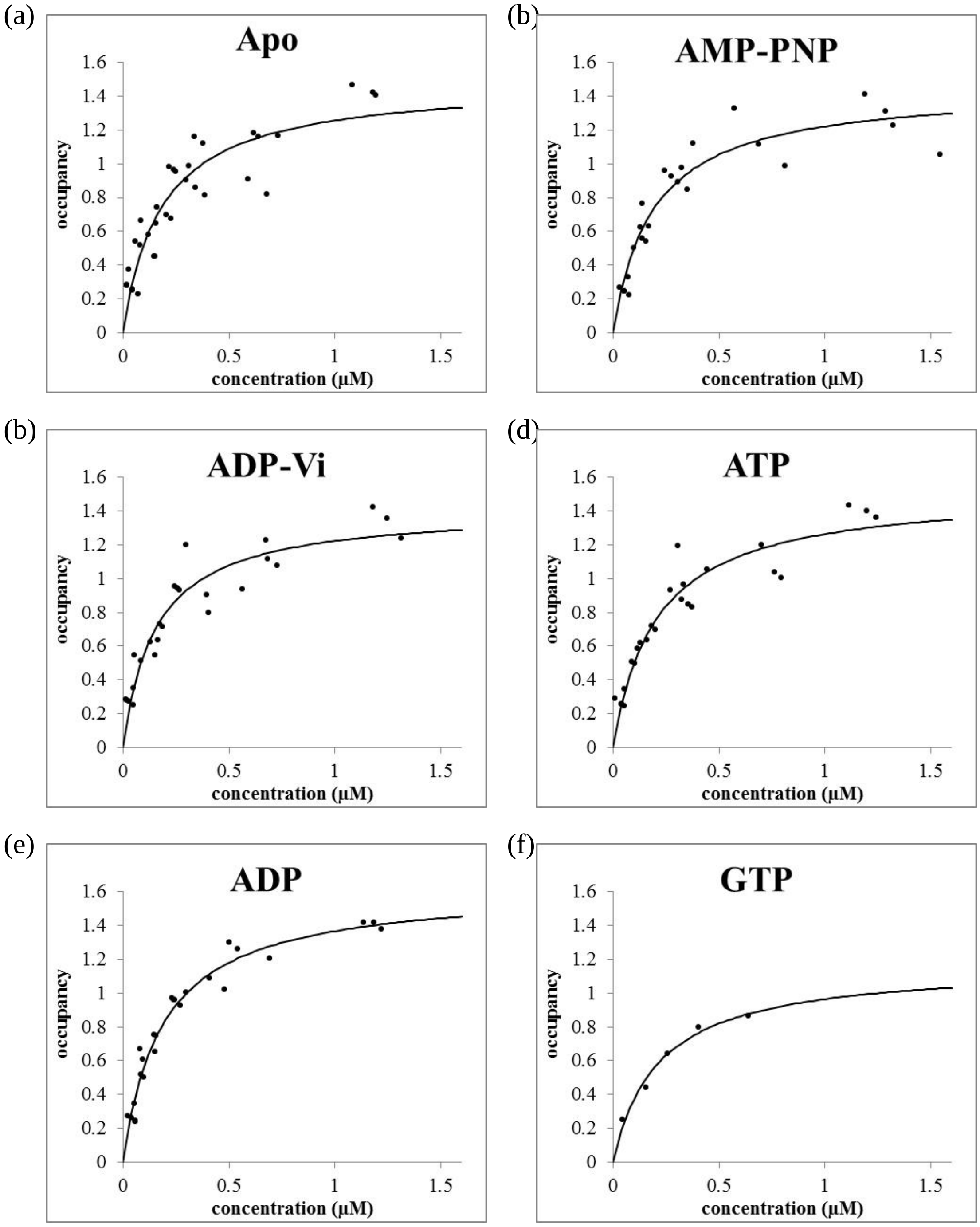

**Figure 3.2 Microtuble binding assay of His-TF-h4st5 constructs**

Assays were performed under (a) apo, (b) AMP-PNP, (c) ADP-Vi, (d) ATP, (e) ADP and (f) GTP conditions.

**Table 3.3 Microtuble binding affinity of h4st5 constructs**

| construct | $K_d$ (μM) | occupancy | $R^2$ |
|---|---|---|---|
| His-TF-h4st5 (Apo) | 0.18 ± 0.035 | 1.5 ± 0.10 | 0.8303 |
| His-TF-h4st5 (ATP) | 0.21 ± 0.032 | 1.5 ± 0.09 | 0.9121 |
| His-TF-h4st5 (AMP-PNP) | 0.19 ± 0.031 | 1.4 ± 0.08 | 0.8945 |
| His-TF-h4st5 (ADP-Vi) | 0.15 ± 0.028 | 1.4 ± 0.08 | 0.8843 |
| His-TF-h4st5 (ADP) | 0.19 ± 0.019 | 1.6 ± 0.06 | 0.9581 |
| His-TF-h4st5 (GTP) | 0.21 ± 0.052 | 1.2 ± 0.11 | 0.9759 |

### 3.2 Crystals of the stalk constructs and their diffraction qualities

Crystals of mDS277-His, mDS277ΔMTBDα–His, mDS277ΔMTBDα and mDS277ΔMTBD+β-His were obtained by hanging-drop vapor diffusion method as described in chapter 2. Photos of these crystals are shown in **Figure 2.9 a-d**.

Crystals of mDS277ΔMTBD+β-His were diffracted to ~8 Å resolution. I considered impossible to determine the structure of mDS277ΔMTBD+β-His because of the limitation of the X-ray diffraction.

Crystals of mDS277ΔMTBDα-His were diffracted to ~7 Å resolution (**Figures 2.8a to 2.8d)**. Molecular replacement was applied to determine the phase angles of these data sets, however no possible solutions were found.

mDS277ΔMTBDα, the protein without His×6 tag, was crystallized with 27.5% 2-Propanol, 5% PEG1000 and 0.1 M Sodium citrate pH 6.0. The diffraction limit of mDS277ΔMTBDα reached to ~2.5 Å (**Figure 2.11)**. Although the diffraction limit has been improved, the dimmed diffraction patterns of mDS277ΔMTBDα with high mosaic values prevent image processing at high resolution.

Crystals of mDS277-His were diffracted to 3.5 Å resolution with glycerol treatment after crystallization (**Figure 2.12a** and **Table 2.2**). Interestingly, crystals treated with 35% PEG3350 were diffracted to 2.5 Å and looks better than those treated with glycerol (**Figure 2.12b** and **Table 2.2**).

### 3.3 Effects of crystal dehydration

As described above, treatment with 35% PEG3350 dramatically improved the diffraction qualities of mDS277-His crystals. Changes of the cell dimensions and symmetries were observed between these two types of crystal. It is considered that the crystal dehydration induced these changes. I tried first to obtain phase information of data sets of dehydrated crystals by molecular replacement using the dynein MTBD structure (PDB ID: 3ERR) as a search model. However, despite the perfect amino acid sequence identity of the MTBD region, I was unable to obtain the correct solution. Then, phase determinations by SAD or MAD method with SeMet derivatives was tried.

Data sets of SeMet derivative near the absorption edge of Se atoms diffracted to 2.9~3.0 Å resolution (**Table 3.4**). The resolution limits and qualities of these data sets seemed sufficient for phase calculations, however both MAD and SAD calculations provided no interpretable solutions. No remarkable anomalous peaks were found in the anomalous difference Patterson maps (**Figure 3.3**). This would be considered that crystal twinning induced by dehydration prevented to solve heavy atom positions. In fact, the value of $|\mathbf{E}^2\text{-}1|$, distributions of L test and H test implied the formation of twinned crystal (**Figure 3.4 and Figure 3.5**). These features were not found in the crystals without dehydration process. This kind of crystal twinning is known as non-merohedral twin accompanying the significant change of diffraction patterns [Dauter, 2003]. Similar features were found in the dehydrated crystals of native mDS277-His; dramatic change of estimated unit cell parameters between the dehydrated crystals and the non-dehydrated ones. Non-merohedral twin is usually fatal for structural calculations because of the difficulty to separate a data set according to the estimated twin fraction. I concluded that dehydrated crystals of mDS277-His are considered as non-merohedral twin that lead to obtain no structural solutions.

Dehydration was performed with increments of polyethylene glycol concentration. First, crystals of mDS277 was incubated 16 hours in 0.15M $NH_4H_2PO_4$, 10% Glycerol and 23~32% PEG3350. In the condition of 23% PEG3350, the crystal diffracted to 3.5 Å resolution. In 24~26% PEG conditions, the diffraction limits lowered under 6 Å. In 28~32% conditions, diffraction limits were recovered depend on PEG concentration and the maximum resolution was 2.5 Å at 32% PEG3350. (**Figure 2.12b**) The initial crystal in 23% PEG condition diffracted as relatively sparse pattern with cell dimension ($a$=$b$=103 Å, $c$=69 Å), while higher PEG conditions in 24~32% did dense patterns that is a feature of dehydrated crystals. These results indicate that the high concentration PEG3350 is effective to dehydrate crystals of mDS277-His and the molecular rearrangements in crystals start under 24% PEG3350 concentration. Judging from the dynamic change of diffraction pattern, partially rearranged molecules decrease the diffraction limits of crystals during the dehydration process, but eventually dehydration tightened molecular packing and increased the diffraction limit again in higher PEG concentration.

**Table 3.4 Crystallographic data of the SeMet derivative crystal.**

| Crystal | SeMet derivative (dehydrated) | | |
|---|---|---|---|
| | Se-Peak | Se-Edge | Se-Remote (high) |
| X-ray Source | BL44XU | BL44XU | BL44XU |
| Space group | $P3_112$ or $P3_212$ | $P3_112$ or $P3_212$ | $P3_112$ or $P3_212$ |
| Unit-cell parameters | | | |
| *a* (Å) | 181.935 | 182.049 | 182.119 |
| *b* (Å) | 181.935 | 182.049 | 182.119 |
| *c* (Å) | 50.600 | 50.618 | 50.627 |
| Wavelength (Å) | 0.97886 | 0.97913 | 0.96391 |
| Resolution range (Å) | 50.00-2.90<br>(2.95-2.90) | 50.00-3.00<br>(3.05-3.00) | 50.00-3.00<br>(3.05-3.00) |
| Total reflection | 444,957 | 440,134 | 429,813 |
| Unique reflections | 21,138 | 19,151 | 19,152 |
| Completeness (%) | 98.6(78.6) | 100(99.8) | 99.9(99.3) |
| $R_{\mathrm{merge}}(I)$ (%)[a] | 8.7(76.8) | 7.5(60.4) | 8.0(70.4) |
| $< I/\sigma(I) >$ | 52.6(1.4) | 67.9(5.6) | 61.9(3.3) |

Values in parentheses are for the highest resolution shells.

[a] $R_{\mathrm{merge}}(I) = \Sigma_{hkl}\Sigma_i |I_i (hkl) - <I (hkl)>| / \Sigma_{hkl}\Sigma_i I_i (hkl)$, where $I_i (hkl)$ is the value of the *i* th measurement of the intensity of reflection *hkl*, $<I (hkl)>$ is the mean value of the intensity of the reflection *hkl* and the summation is the overall measurement.

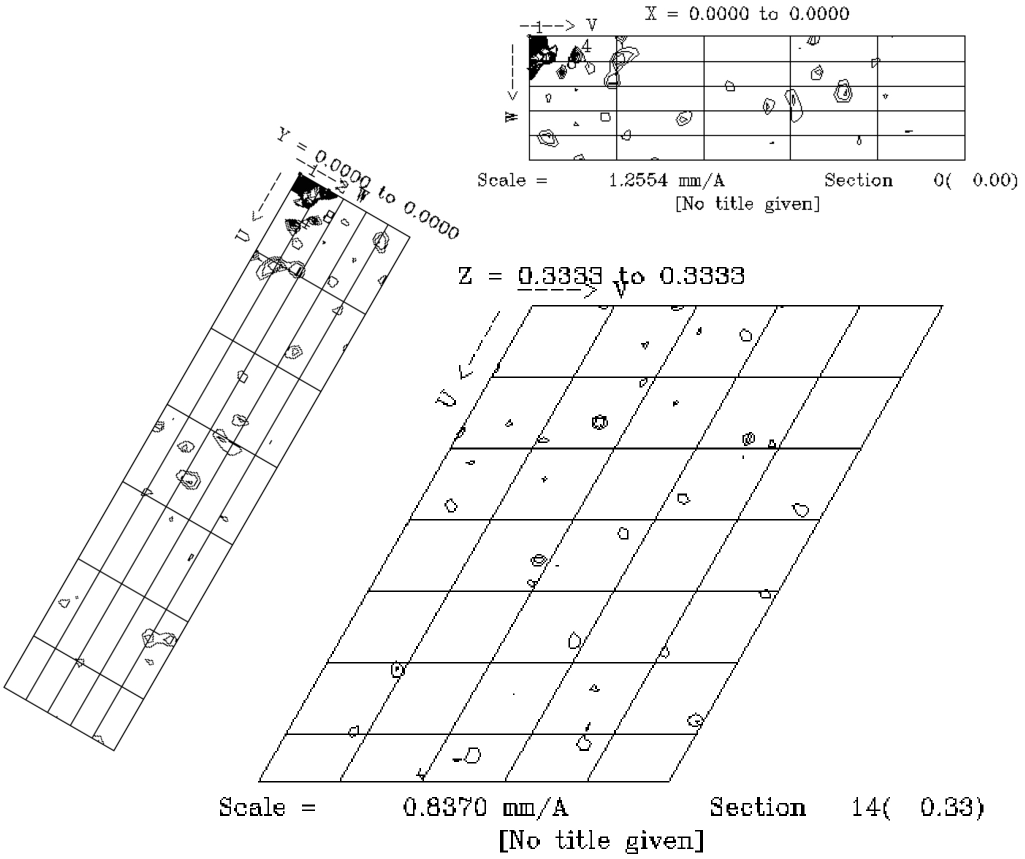

**Figure 3.3 Anomalous difference Patterson maps of dehydrated SeMet derivative**

Top: The map depicted in $u$ = 0 section

Bottom, left: The map depicted in $v$ = 0 section

Bottom, right: The map depicted in $w$ = 1/3 section

These maps were generated from the peak data set of Se atom by FFT of CCP4 program suite at 5.0 Å resolution [Immirzi, 1973; TenEyck, 1972]. The maximum value was normalized to 100 and contours were drawn at intervals of 1 starting from 1.

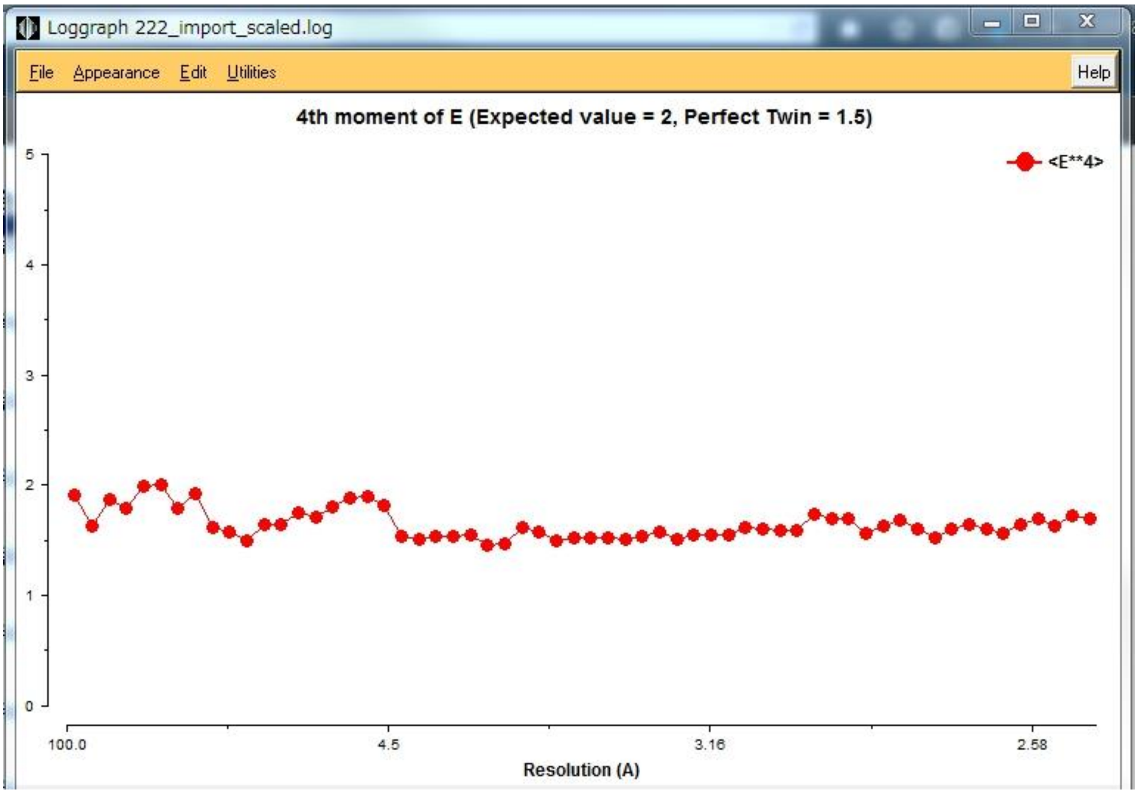

**Figure 3.4 Distribution of 4th moment of E calculated from the data set of dehydrated crystal**

The diagrams of **Figure 3.4** and **Figure 3.5** were calculated from the 2.5 Å data set of dehydrated crystal showed in Table 2.2 by TRUNCATE of CCP4 program suite [French *et al*., 1978].

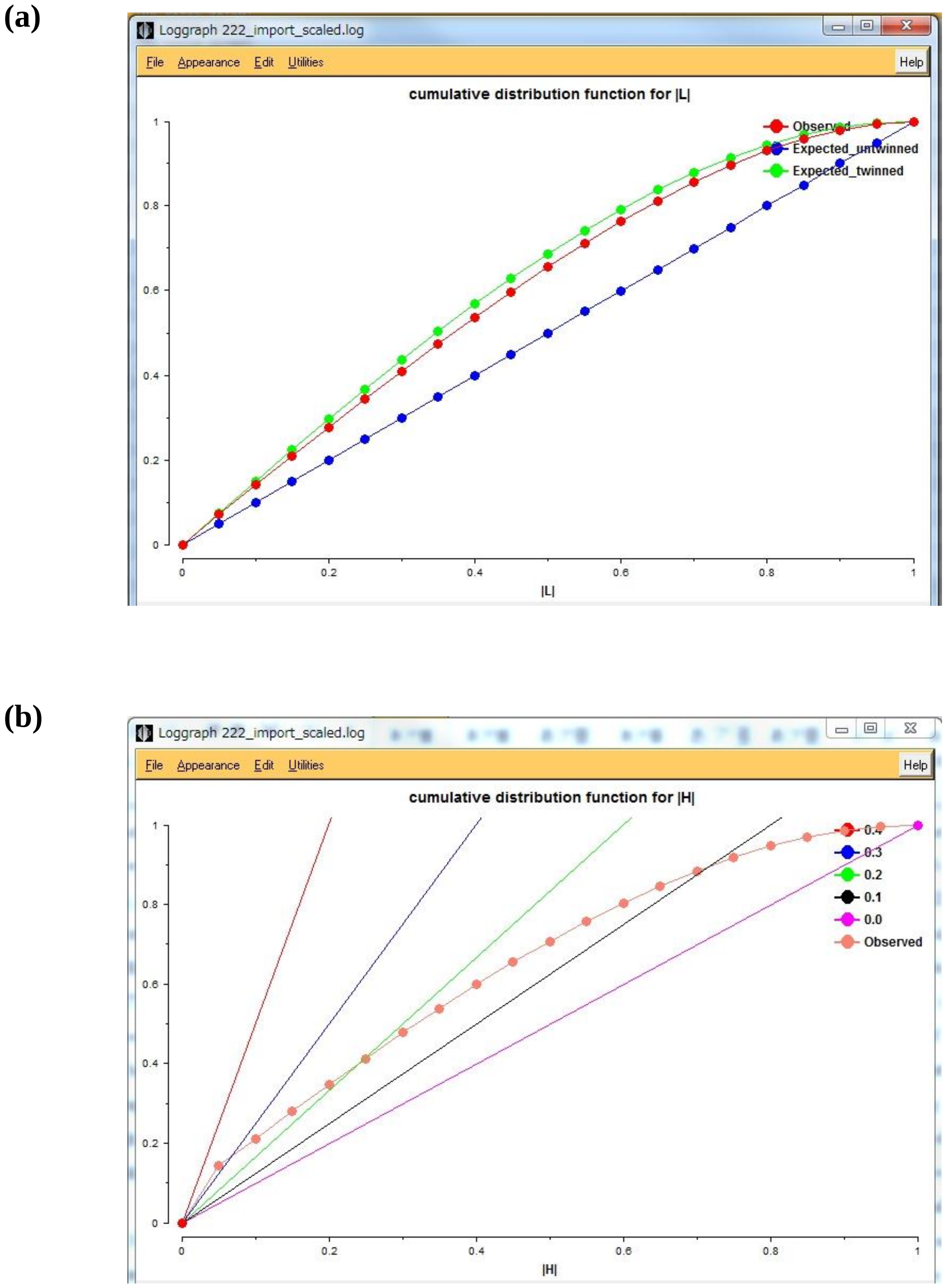

**Figure 3.5 Twinning test Diagram of data set of dehydrated crystal**

Cumulative distributions of L test (a) and H test (b). (a) The theoretical untwinned distribution, theoretical twinned one and observed were represented in blue, green and red respectively. (b) Theoretical distributions of twin fractions of 0.0, 0.1, 0.2, 0.3 and 0.4 were showed in magenta, black, green, blue and red respectively and the observed in light salmon.

## 3.4 Overall structure of mDS277-His

The mDS277-His structure was determined from the non-dehydrated crystals by SAD. The refined 3.5 Å resolution structure contains 263 residues modeled from Thr3209 to Asn3471. Two residues in the N terminal and 18 residues in the C terminal, including the poly-His tag, were not visible in the electron density map. The crystal structure of mDS277 comprises 8 helices. The two long N-terminal and C-terminal helices formed an extended antiparallel coiled coil (outward CC1 and inward CC2 helices), and the residual 6 helices (designated H1 to H6 in the SRS-MTBD structure) [Carter *et al.*, 2008] formed a globular domain (MTBD) at the distal end of the stalk (**Figure 3.6a**). The arrangement of the secondary structure was the same as that of the SRS-MTBD fusion protein reported in 2008 [PDB ID: 3ERR] **(Figure 3.6b)**, except that the CC1 and CC2 helices were twice as long. The CC1 helix is 6 residues longer compared with the CC2 in mDS277-His so that the proximal end of the stalk coiled coil is staggered. Comparison of the structure of mDS277-His and SRS-MTBD yielded an averaged root-mean square deviation (RMSD) of 1.2 Å in $C^{\alpha}$ atoms when superimposed from residues GluE3260 to LysK3427. When checking the difference along the sequence, the $C^{\alpha}$ atoms with relatively high RMSD values (~3 Å) are seen in CC1, CC2, and loops in MTBD **(Figure 3.7)**.

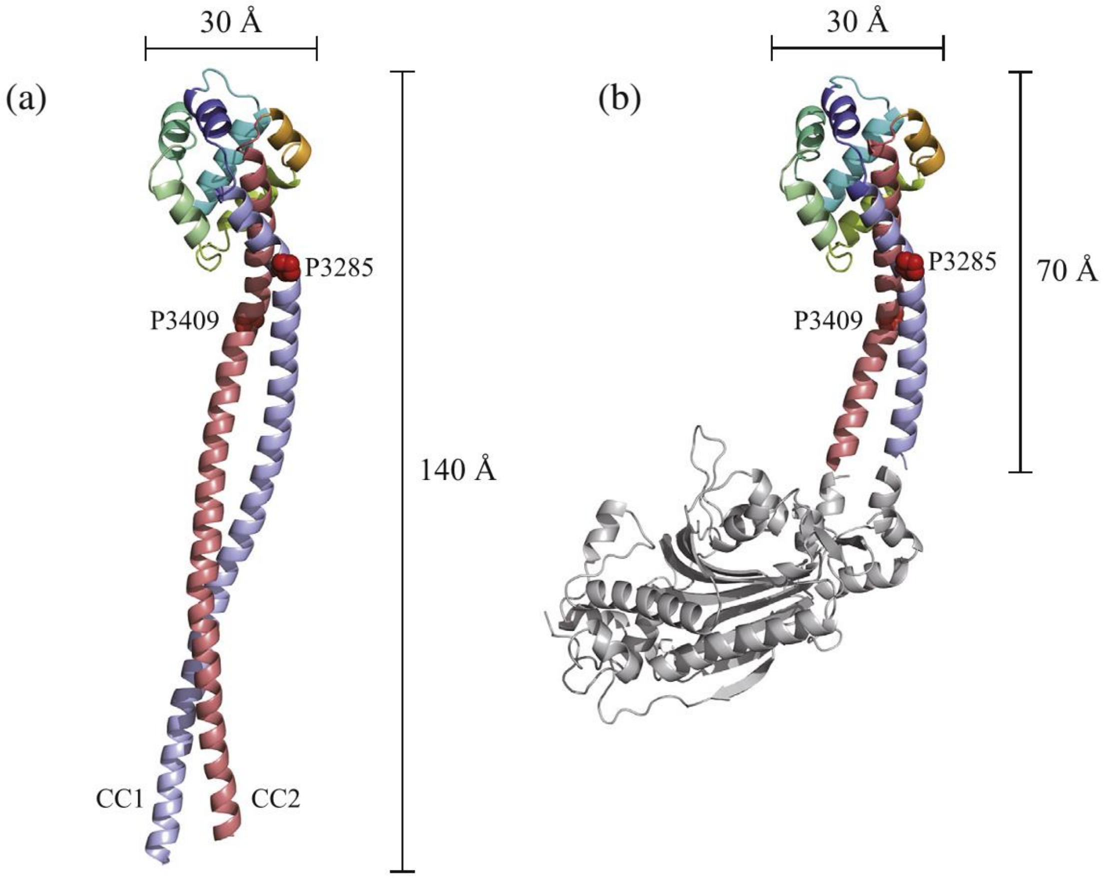

**Figure 3.6 Structures of mDS277-His and the SRS-MTBD fusion protein.**

(a) Crystal structure of mDS277-His. The ribbon diagram is colored red to blue along the sequence from the N- to C-terminus, and two conserved prolines (Pro3285 and Pro3409) are drawn as CPK models. (b) Crystal structure of the SRS-MTBD fusion protein (PDB code 3ERR). The colors of the ribbon diagram are the same as shown in (a). The fused SRS portion is gray.

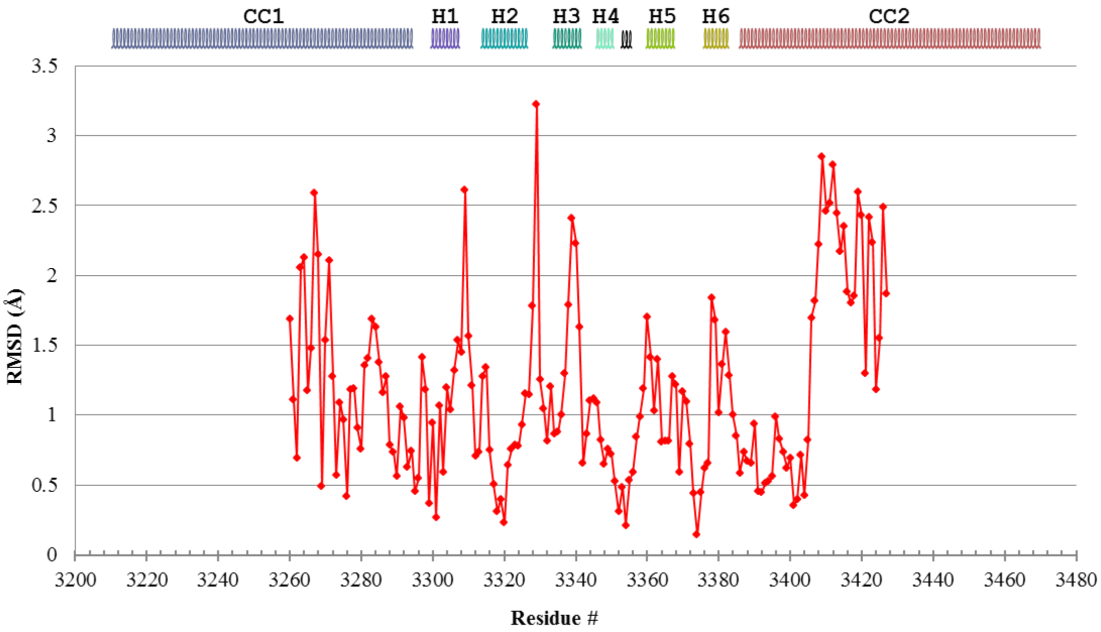

**Figure 3.7 Distribution of RMSD values between mDS277-His and SRS-MTBD along the sequence.**

Plotted dots are RMSD of each $C^{\alpha}$ atoms in comparable residues (Glu3260-Lys3427) between mDS277-His and the SRS-MTBD fusion protein. Upper is the distribution of α-helices detected from the structure of mDS277-His. The detection of secondary structures were carried out by DSSP server [Kabsch *et al*., 1983]

### 3.5 Coiled-coil registry of mDS277

A change in the stalk coiled-coil registry is a key to tune the affinity of MTBD for microtubules along with the ATP hydrolysis activity [Kon *et al.*, 2009]. I assessed the interaction between two helices using SOCKET software to detect knobs-into-holes packing of the coiled coil [Walshaw *et al.*, 2001]. One antiparallel coiled-coil packing arrangement comprising Leu3227–Asp3279 in the CC1 helix and Val3407–Ile3459 in the CC2 helix was detected in the structure of mDS277-His. Twenty-seven amino acid residues (13 from CC1 and 14 from CC2) were involved in the interaction (**Figure 3.8**). Use of TWISTER software confirmed that the entire stalk has a canonical coiled-coil structure without any irregular interactions such as skips or stutters [Strelkov *et al.*, 2002]. Based on this analysis and a comparison between available structures [Carter *et al.*, 2008, PDB ID: 3ERR; Kon *et al.*, 2012, PDB ID: 3VKG], the registry of mDS277-His was confirmed as "+β" (**Figure 3.9a, 3.9b**), which corresponds to the low affinity microtubule and low ATPase state and shifts half heptad from the structure of the full-length motor domain [Kon *et al.*, 2012, PDB ID: 3VKG], whose stalk coiled coil exhibited "α" registry (**Figure 3.9c**). Moreover, the register of +β was distributed across the entire coiled coil. Specifically, the N-terminus of the CC1 helix almost reached the region interacting with the strut, the coiled coil structure extends from AAA5 domain (**Figure 1.5**), corresponding to Glu3296 in the structure of ΔMTBD-A of the dynein motor domain from *D. discoideum* (**Figure 3.9a, 3.9c**).

Together with the ADP-bound structure with high affinity for microtubules [Kon *et al.*, 2012], two independent structures before and after the helix slide has now become available. However, structural basis for switching between these two structural states is still elusive, and there is no structural characterization of the state transition between α and +β using a same construct. Locking the specific registrations of the coiled coil is achieved by oxidation of disulfides of paired cysteine residues introduced into two helices [Kon *et al.*, 2009]. Therefore, I performed SDS-PAGE and CD spectra measurements of double-cysteine mutant of mDS277-His. The mutant named mDS277α-His was locked in either registry of α or +β with and without disulfide bond

(**Figure 2.14**). Conversion of the registry has been confirmed by electrophoretic mobility shift assay. An oxidation-induced mobility shift was observed between reduced protein mDS277α-$\text{His}_{\text{R}}$ and oxidative treated mDS277α-$\text{His}_{\text{Ox}}$. Both spectra of mDS277α-$\text{His}_{\text{R}}$ and mDS277α-$\text{His}_{\text{Ox}}$ exhibited typical patterns of α-helix rich protein with remarkable peaks at the wavelength of 208 nm and 222 nm. The $[\Theta]_{222\text{nm}}$ of mDS277α-$\text{His}_{\text{R}}$ was same to mDS277-His, while the $[\Theta]_{222\text{nm}}$ of mDS277α-$\text{His}_{\text{Ox}}$ was decreased after cross-linkage. The ratio of $[\Theta]_{222\text{nm}}$ (mDS277α-$\text{His}_{\text{R}}$) / $[\Theta]_{222\text{nm}}$ (mDS277α-$\text{His}_{\text{Ox}}$) was 1.12. This means that the helical content of mDS277-His increased by 12% upon reduction of engineered disulfide bond.

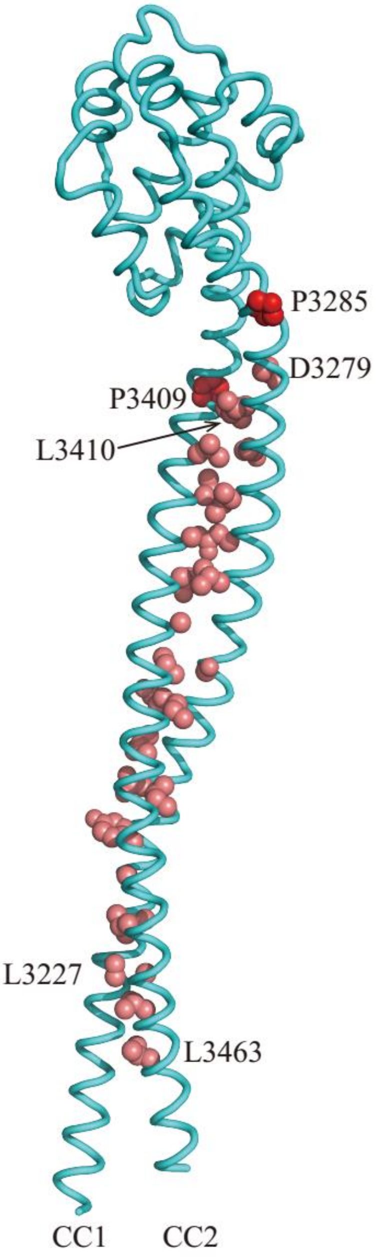

**Figure 3.8 Knobs-into-holes side-chain packing in mDS277-His.**

Side chains of residues, assigned as knobs, are shown as pink space-filling models. Two conserved proline residues are also shown as a reference in red.

**(a)**

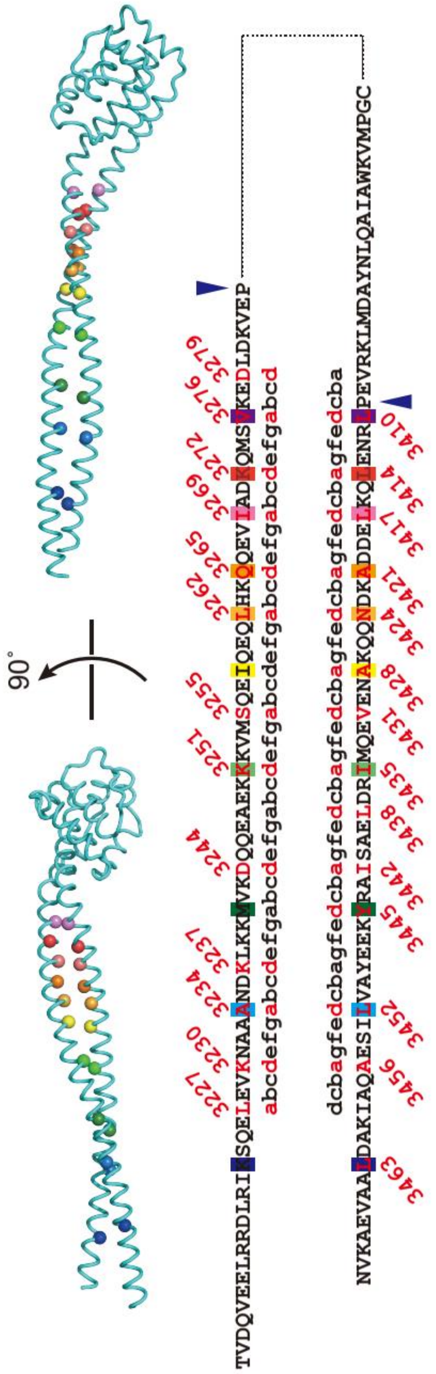

**Figure 3.9 Comparison of the heptad register of the stalk coiled coils.**

(a) mDS277-His Residues assigned as knobs are shown in red one-letter amino acid codes. Rainbow-colored spheres on the ribbon models show the positions of the $C^{\alpha}$ of the corresponding residues in the alignment. Blue arrowheads indicate the conserved proline residues.

**(b)**

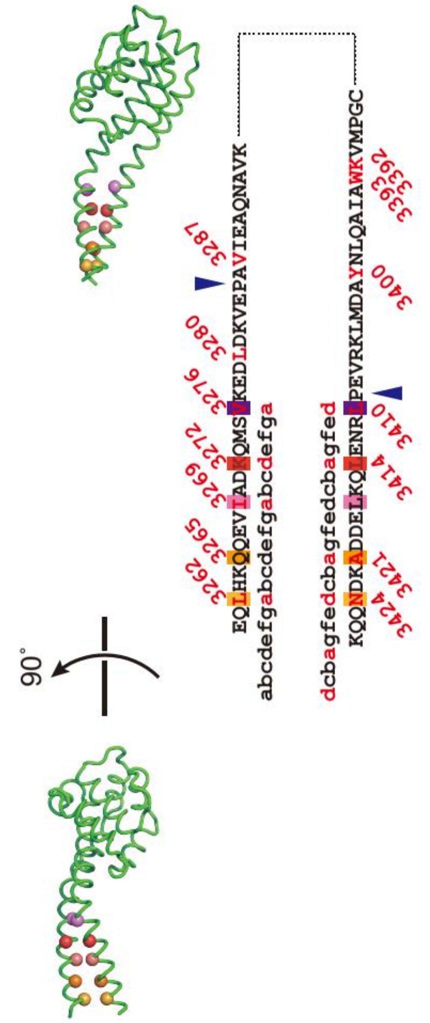

**Figure 3.9 Comparison of the heptad register of the stalk coiled coils.**

(b) SRS-MTBD fusion protein. Residues assigned as knobs are shown in red one-letter amino acid codes. Spheres colored in yellow to magenta on the ribbon models show the positions of the $C^{\alpha}$ of the corresponding residues in the alignment. Blue arrowheads indicate the conserved proline residues.

**(c)**

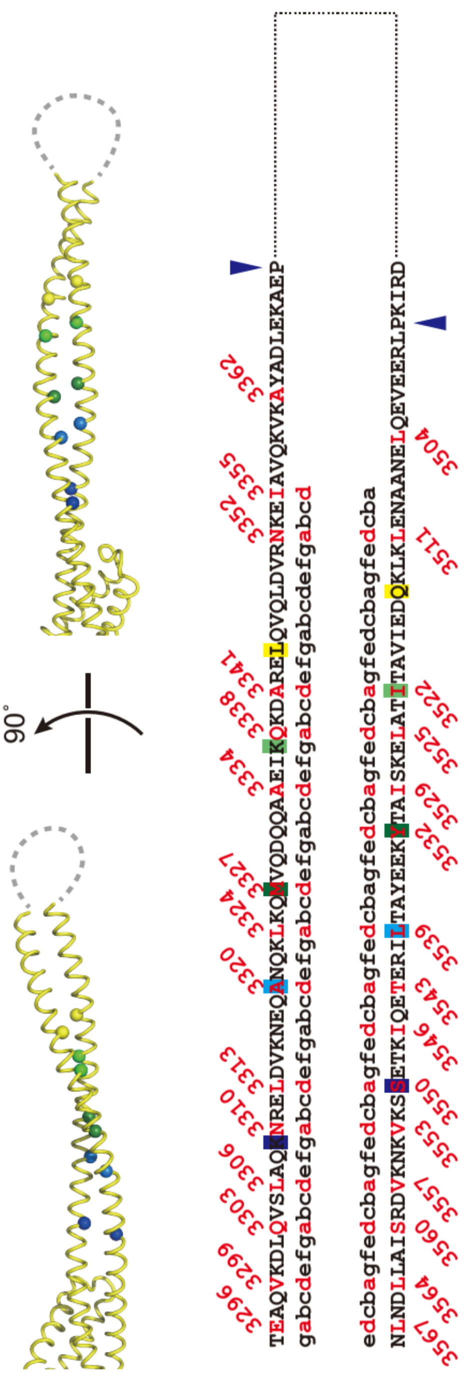

**Figure 3.9 Comparison of the heptad register of the stalk coiled coils.**

(c) stalk region of the ΔMTBD-A molecule of the dynein motor domain. Residues assigned as knobs are shown in red one-letter amino acid codes. Spheres colored in yellow to blue on the ribbon models show the positions of the $C^{\alpha}$ of the corresponding residues in the alignment. Blue arrowheads indicate the conserved proline residues.

## 3.6 Molecular dynamics simulations

Based on the CD spectra, cysteine-introduced mDS277-His variant held high helical content before and after the registry shift. It seems obviously energetically unfavorable to break the knobs-into-holes packing interaction while sliding as rigid tubes for two coiled-coil helices accompanying the rearrangement of extensive knobs-into-holes packing. To investigate thermodynamic stability and to capture the motion of the stalk in aqueous solution, molecular dynamic (MD) calculations were performed. Initially, I performed a 50-ns canonical MD simulation for the wild type mDS277 at 300 K. After 40 ps, the RMSD of non-hydrogen main chain atoms varied from 2 Å to 11 Å (**black line in Figure 2.15**). The result shows that the stalk structure moved widely between near-X-ray and other structures (**Figure 3.10**).

From the results of principle component analysis for the MD trajectory, I found that the directional fluctuation of the MTBD region originated from the conserved Pro residues in both helices (Pro3285 in CC1 helix and Pro3409 in CC2 helix) (**Figure 3.11a**). When I compared the simulated structures picked up with a 10-ns interval based on the superposition of the MTBD region, the stalk coiled coil seemed to oscillate (**Figure 3.11a**). Alignment of these simulated stalk coiled-coil structures with the structure of the dynein motor domain (PDB ID: 3VKG) shows that the hypothetical oscillating plane of mDS277 is almost parallel to the AAA$^+$ ring (**Figure 3.11b**). Therefore, the MTBD fluctuated in one direction without rotation along the long axis of the coiled coil.

The first principle component of the MD trajectory of the stalk helices was characteristic and coincident with the helix sliding model (**Figure 3.12a**). The fluctuation was oriented toward the base of the stalk coiled-coil so that although the two helices fluctuated like a piston, the phases of the motion of the two helices were synchronized, and each stroke was insufficient to cause the registry shift within the unbiased MD calculation. Because the starting point of the oriented fluctuations of the stalk coiled coil was the two conserved proline residues, we also carried out a 50-ns simulation from the homology model of the Pro3285Ala/Pro3409Ala double mutant under the same conditions. The RMSD of backbone heavy atoms fluctuated from 2 Å to 12 Å (**red line in Figure 2.15**) after 80 ps. Therefore, the thermodynamic stability of the double mutant is similar to that of the wild type.

Interestingly, the first principle component of the MD trajectory of the mutant mDS277-His in **Figure 3.12b** showed a completely different feature compared with wild-type mDS277-His. Fluctuation of the MTBD region includes random rotation along the long axis of the stalk with consequent loss in directional movement parallel to the face of the AAA$^+$ ring. Moreover, the mode of oscillation and the structure of the simulated coiled coil were significantly altered in the mutant mDS277-His. Therefore, the information obtained from the simulated structures indicates that the two long helices of the mutant mDS277-His bend with an associated loss of oriented fluctuation instead of moving like a piston (**Figure 3.12b**).

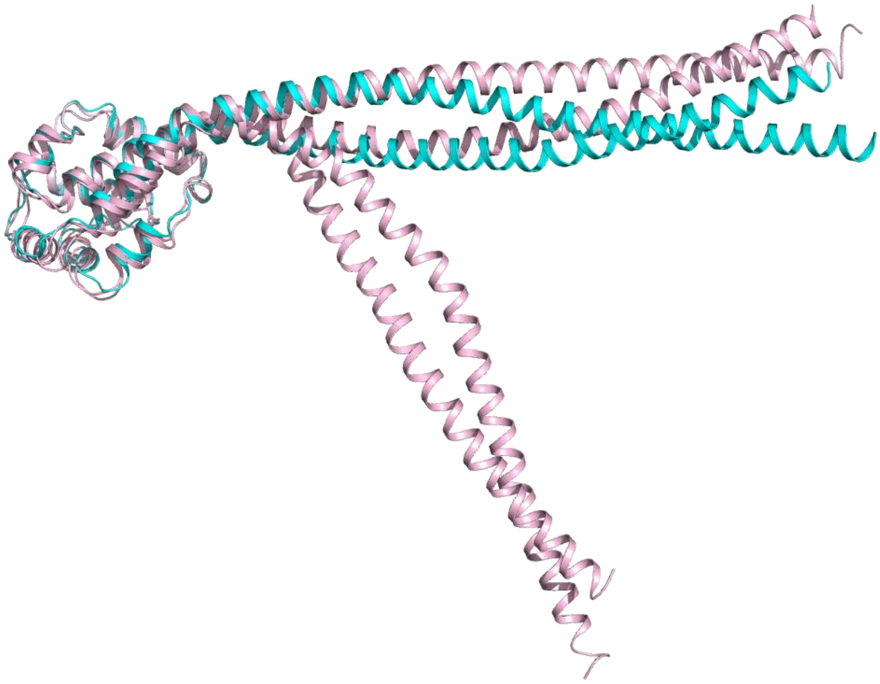

**Figure 3.10 Superimposed models of X-ray structure (cyan) and simulated structure (magenta) with maximum deviation from X-ray structure.**

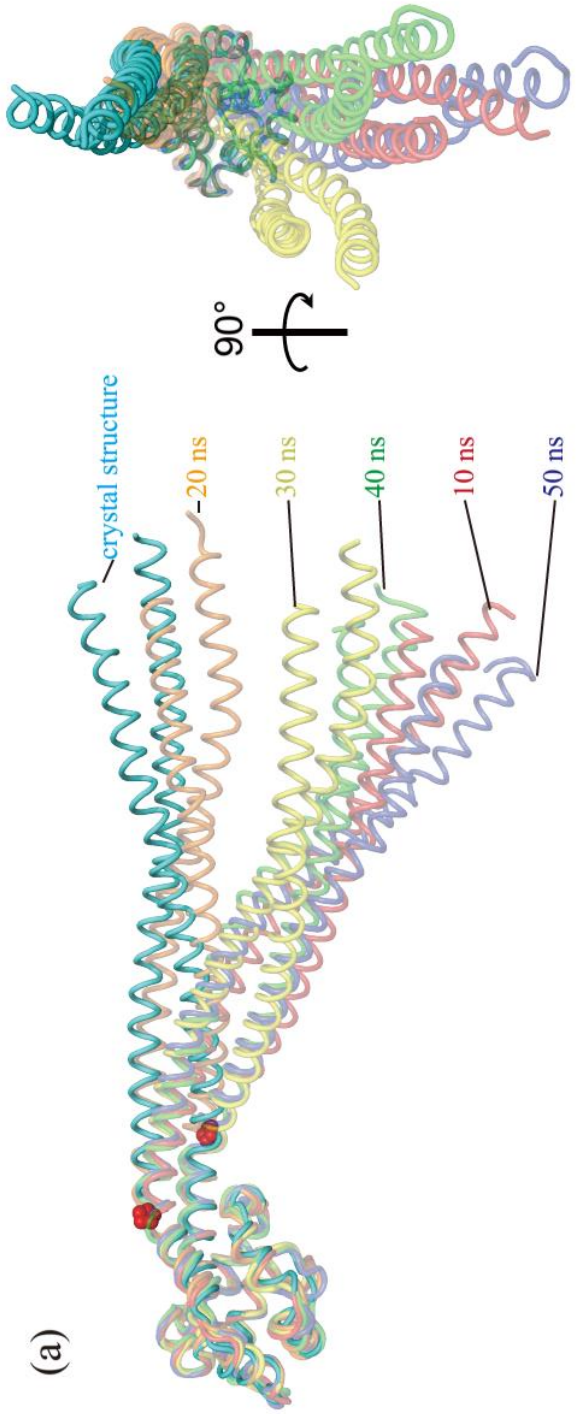

**Figure 3.11 Swing motion of the MTBD.**

(a) Five simulated structures are superimposed on the crystal structure. The two conserved proline residues are shown as red space-filling models.

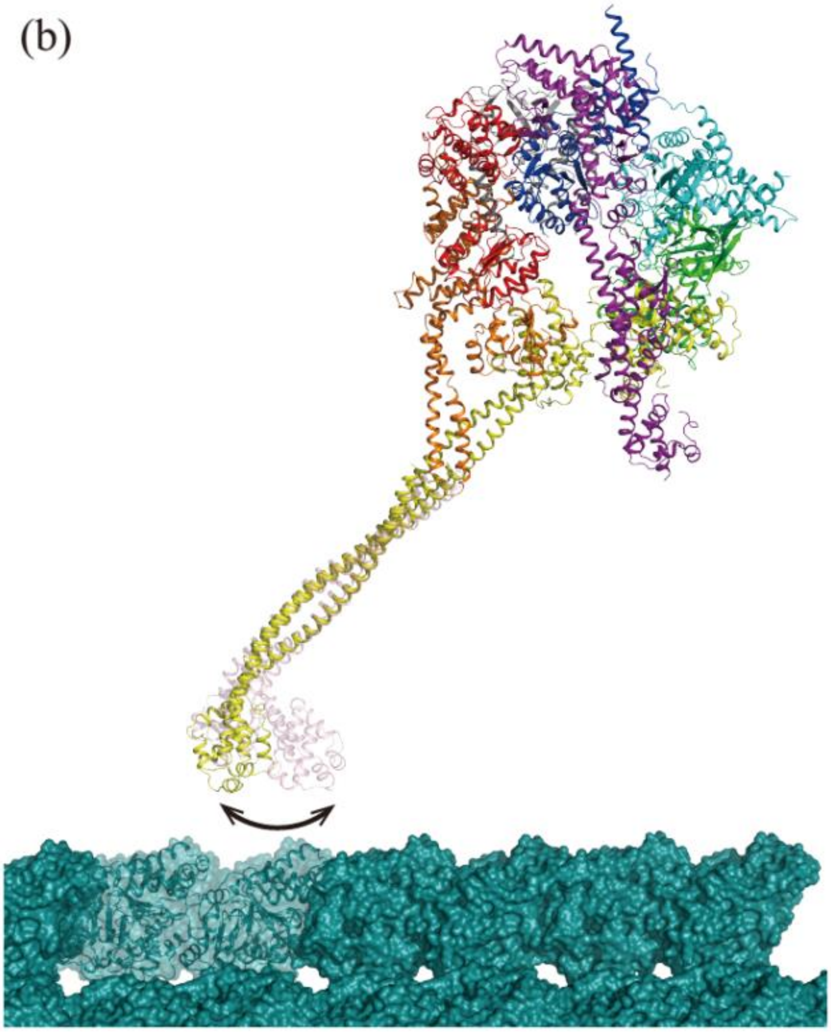

**Figure 3.11 Swing motion of the MTBD.**

(b) Superimposed model of the dynein motor domain overlapped with the simulated Stalk277 structures. The orientation of the swing is parallel to the AAA ring and is consistent with a diffusive search-like motion for the next step along the MT.

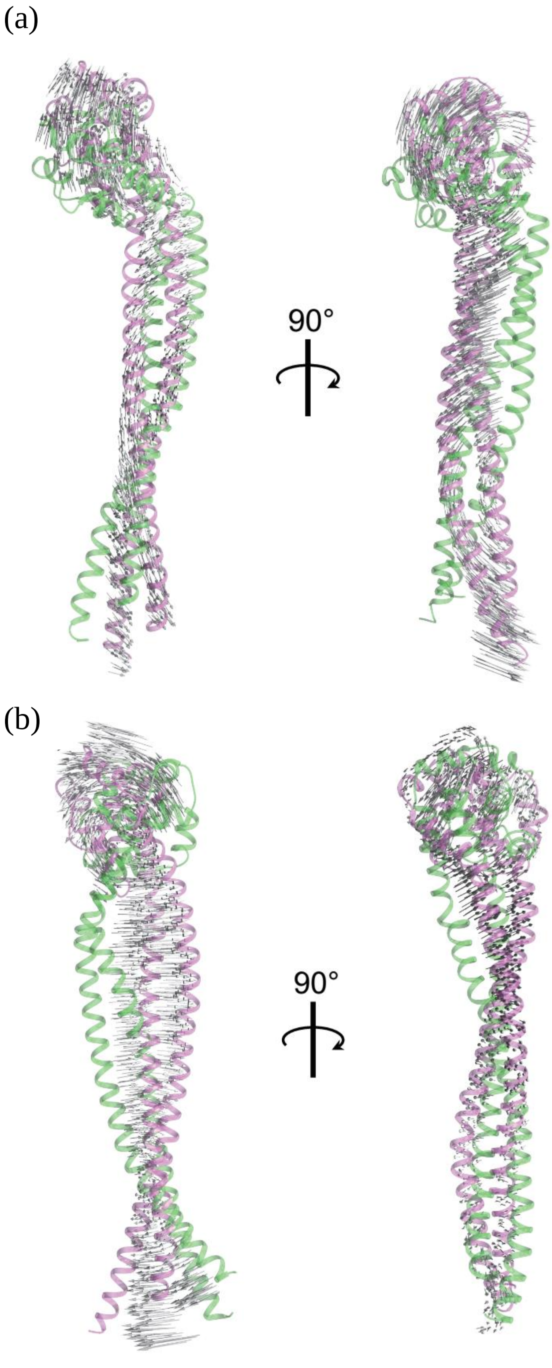

**Figure 3.12 Principle component analysis of MD trajectory.**

(a) The first component of the wild-type structure. Small arrows indicate the direction of the motion. (b) The first component of the P3285A/P3409A mutant protein. Green and purple models show maximum displacements among the simulated structures. The arrows correspond to the eigenvector of the first principal component. This figure was illustrated by UCSF chimera [Pettersen *et al*., 2004]

# Chapter 4

# General discussion

## 4.1 Significance of the structural studies on mDS277

Although the resolution of the present mDS277-His structure is limited to 3.5 Å, there were no ambiguities for assigning the positions of residues throughout the molecule in the $2F_o$-$F_c$ electron density map. Moreover, the anomalous signals originating from the Se atoms in the anomalous difference Fourier map were easily recognized, and the positions of the corresponding peaks were consistent with the positions of the methionine residues (**Figure 2.13**). The structure of mDS277-His is similar to that of SRS-MTBD. However, the coiled-coil region of mDS277-His is 70 Å longer than that of SRS-MTBD and includes most of the stalk region, revealing that the entire stalk region possesses the canonical coiled-coil structure with the registry of +β.

In addition, the CD spectra of mDS277α-His with and without disulfide bond confirmed that highly helical characteristics of the entire stalk region were rather conserved in the α registry. In contrast to other common examples such as open-closed or ordered-disordered structures, it is very rare for two long helices to form an alternative stable coiled-coil conformation. However, the structural basis for energetically unfavorable helix sliding of the dynein stalk remains unclear.

The signal generated by this helix sliding coupled to a change in registry should be transmitted to the $AAA^+$ ring. Note that the N-terminal end of mDS277-His with +β registry reached the region that interacts with the strut. Evidence indicates that the strut coiled-coil serves as a possible two-way communication path [Kon *et al.*, 2012]. Indeed, my structure of mDS277-His supports the "Helix sliding hypothesis" [Gibbons *et al.*, 2005].

Because the structure of mDS277-His is more complete compared with other available structures, it serves as a suitable starting model for performing MD simulations. MD simulation has revealed interesting features of the MTBD and the stalk coiled coil. We performed independent MD simulations starting from two models: (i) the crystal structure of mDS277-His, and (ii) the homology model with the conserved proline residues replaced by alanine. The simulated structures maintained the +β registry during a 50-ns simulation, showing that the stalk fragment is energetically stable. NMR or thermostability studies of MTBD with a short stalk coiled-coil demonstrated that +β registry of coiled coil corresponds to the low-energy conformation [McNaughton *et al*., 2010; Carter *et al*., 2008]. This is consistent with the result of CD spectra from mDS277-His showing that helical content of mDS277-His with the +β registry is slightly higher than that with the α registry (mDS277α-His).

Furthermore, the results of principal component analysis clarify the intrinsic structural properties. The first components of the MD trajectories occupy approximately half of the total of mDS277-His and the P3285A/P3409A mutant (48.3% and 49.1%, respectively). The first components represent large-scale motions, that of wild-type mDS277-His is significantly biased. The biased fluctuation is parallel to the AAA$^+$ ring and along the long axis of the microtubule, which makes us imagine that the protein is searching for a new binding site on the microtubule by this motion (**Figure 3.11b**).

Another important difference between the conformations of mDS277-His and the mutant protein is the piston-like motion of the coiled-coil region. In wild-type mDS277-His, the two coiled-coil helices oscillate along the longest axis of the stalk in the “helix-sliding directions” while the P3285A/P3409A mutant model does not (**Figure 3.12**). Substitution of the two conserved proline residues with alanine residues altered the orientation and amplitude of the biased fluctuation, which implies that the conserved proline residues in CC1 and CC2 are critical for the directional motion of the MTBD.

This clear and significant difference indicates that the conserved proline residues convert the structural flexibility of the coiled coil into conformational changes that couple with the registry shift (i.e., akin to the crankshaft of an internal combustion engine). My results emphasize the structural importance of the two conserved proline residues.

## 4.2 New structural model of stalk-mediated communication

The comparison of the X-ray structure presented here and those of previously reported gives us an interesting insight into stalk-mediated communications. Current structure is similar to that of the low-affinity MTBD (PDB ID: 3ERR-A). When compared with the MTBD using only the relative positions of the two conserved Pro residues (Pro3285 and Pro3409), the distances between the two proline residues are quite similar for mDS277-His (22.0 Å) and SRS-MTBD (22.9 Å). However, when I compared current structures with the rigid-body docking model of the low-affinity MTBD structure (PDB ID: 3J1U) and the pseudoatomic high-affinity MTBD structure (PDB ID: 3J1T) [Redwine *et al.*, 2012], there were some significant differences (**Figure 4.1**).

In the proposed two-way communication model of the EM analysis, the transition to a high-affinity conformation involves a large displacement of H1 and an opening of CC1 helices at the distal end of the stalk. In the superimposed models of **Figure 4.1a**, the CC2 helix, including the conserved Pro3409, does not differ significantly and appears to act as an anchor upon binding to microtubules. However, comparison of the current most stable MD-simulated structure with the low-affinity MTBD structure and the pseudoatomic high-affinity MTBD structure shows that the orientation of the coiled-coil region becomes more oblique (**Figure 4.1b**). Furthermore, the relative positioning of the conserved Pro3285 on CC1 was similar to that of the high-affinity MTBD model even without repositioning the H1 helix, which is proposed to be a trigger of registry shift in the previous two-way communication model.

These findings suggest a modification to the model proposed previously for the coordination of the nucleotide state and microtubule binding by dynein [Redwine *et al.*, 2012]. I would like to propose a new structural model for two-way communication between MTBD and ATPase domains (**Figure 4.2**). First, molecular dynamics simulation suggests that the CC1 and CC2 helices oscillate together intrinsically before binding to microtubules. Second, upon binding, the anchoring of the CC2 helix to the microtubule might disrupt the synchronized fluctuation of both CCs together with the newly formed intramolecular interactions between a microtubule and the MTBD. Finally, this disruption of synchronization could trigger a registry shift from +β to α.

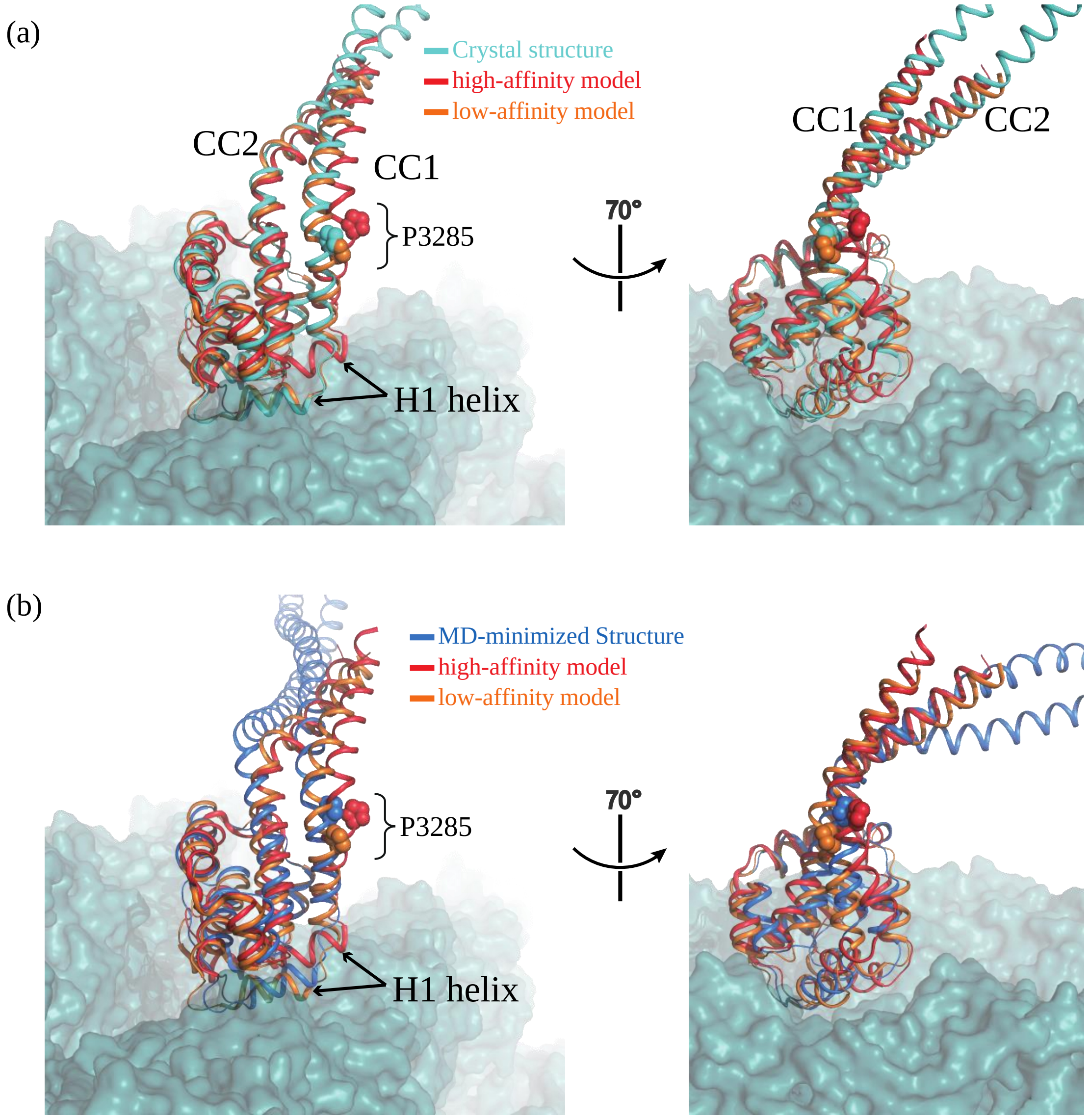

**Figure 4.1 Stalk models superimposed on the MT. Right panels and left panels show side and front views, respectively.**

(a) Crystal structure of mDS277-His in cyan is superimposed on the two EM structures with +β registry colored in orange (PDB ID 3J1U) and red α registry (3J1T). The conserved proline residue in CC1 is shown as a space-filling model. (b) The most stable MD simulated structure was superimposed as described in (a).

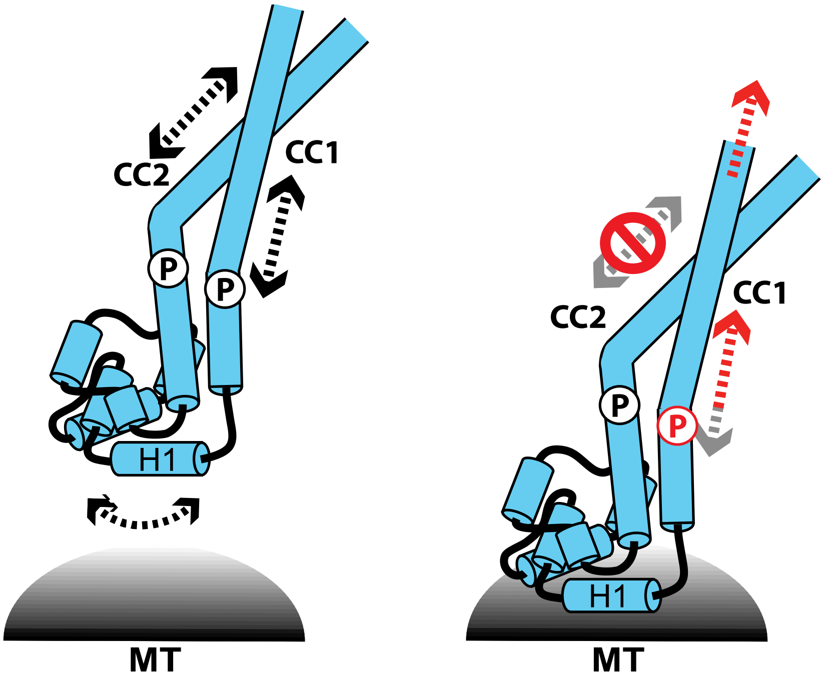

**Figure 4.2 New molecular model for the registry shift caused by MT binding.**

# Chapter 5

## Summary

Dyneins are large microtubule-based motor complexes (over 1000 kDa) that power a wide variety of cellular processes through the coordinated action of a number of subunits. The motor domain is located in the dynein heavy chain and consists of an N-terminal linker of mechanical element, a central ring of six $AAA^+$ modules four of which bind and hydrolyze ATP, and a long stalk extended from the $AAA^+$ ring that has a microtubule-binding domain (MTBD) at its tip. The domain organization of dynein has been revealed by EM and, more recently by X-ray crystallographic studies.

A crucial mechanism underlying the motile activity of cytoskeletal motor proteins is precise coupling of ATPase with track binding activities. In dynein, the stalk region separates these two domains responsible for each activity with a long (>10 nm) anti-parallel coiled-coil, so that it must mediate communication between them. Previous functional studies have provided evidence that this communication is mediated by small amount of helix sliding in the coiled-coil. However, no crystal structure of the entire stalk region including an MTBD was available so far.

In this study, I have tried to analyze the structure of the entire stalk region by X-ray crystallography and the microtubule binding activity by co-sedimentation. Crystal structure of the mouse cytoplasmic dynein's entire stalk (including both MTBD and stalk coiled-coil) was determined at 3.5-Å resolution by the SAD method. This structure together with the previously reported structures of dynein motor domain establishes that the entire stalk can assumes two distinctive coiled-coil conformations (α and +β registries) without a kink in the helix or uncoiling.

In my PhD studies, helical content of the entire stalk region with two different registries (α and +β) was estimated by CD spectra analysis. From the result of CD measurement, the stalk structure with the +β registry, which exhibits low affinity for the microtubule and the low ATPase state should be also considered the ground state.

Furthermore, the result of MD simulation has indicated that the structure of mDS277-His with the longer coiled coil was stable even without other structures such as the SRS. I also show completely different motions between the wild-type stalk and its alanine double mutant (whose conserved proline residues were replaced to alanine) obtained from MD simulations followed by principal component analysis, which may be relevant to the stalk-mediated communication.

In this study, the results strongly support the helix-sliding model based on the complete structure of the dynein stalk with canonical coiled-coil packing that exhibits a different form from the structure of the full-length dynein motor domain. I propose a plausible mechanism of helix sliding together with further analysis using molecular dynamic simulations, however further studies, such as the structural analysis of the entire stalk region with the α registry and the motility assay with the motor domain mutated to conserved proline residues are necessary for understanding the stalk mediated two-way communication mechanism of dynein.

## References

Adams, P.D., Grosse-Kunstleve, R.W., Hung, L.W., Ioerger, T.R., McCoy, A.J., Moriarty, N.W., Read, R.J., Sacchettini, J.C., Sauter, N.K., and Terwilliger, T.C. (2002). PHENIX: building new software for automated crystallographic structure determination. *Acta Crystallogr* D Biol Crystallogr 58, 1948-1954.

Afonine, P.V., Grosse-Kunstleve, R.W., Echols, N., Headd, J.J., Moriarty, N.W., Mustyakimov, M., Terwilliger, T.C., Urzhumtsev, A., Zwart, P.H., and Adams, P.D. (2012). Towards automated crystallographic structure refinement with phenix.refine. *Acta Crystallogr* D Biol Crystallogr 68, 352-367.

Arakawa, T., Kamiya, N., Nakamura, H., Fukuda, I. (2013). Molecular dynamics simulations of double-stranded DNA in an explicit solvent model with the zero-dipole summation method. *PLoS ONE* 8:e76606.

Asai, D.J., and Koonce, M.F. (2001). The dynein heavy chain: structure, mechanics and evolution. *Trends in Cell Biology* 11, 196-202.

Berendsen, H.J.C., Postma, J.P.M., van, Gunsteren, W.F., DiNola, A., Haak, J.R. (1984). Molecular dynamics with coupling to an external bath. *J Chem Phys* 81:3684–90.

Burgess, S.A., Walker, M.L., Sakakibara, H., Knight, P.J., and Oiwa, K. (2003). Dynein structure and power stroke. *Nature* 421, 715-718.

Carter, A.P., Cho, C., Jin, L., and Vale, R.D. (2011). Crystal structure of the dynein motor domain. *Science* 331, 1159-1165.

Carter, A.P., Garbarino, J.E., Wilson-Kubalek, E.M., Shipley, W.E., Cho, C., Milligan, R.A., Vale, R.D., and Gibbons, I.R. (2008). Structure and functional role of dynein's microtubule-binding domain. *Science* 322, 1691-1695.

Castoldi, M., and Popov, A.V. (2003). Purification of brain tubulin through two cycles of polymerization-depolymerization in a high-molarity buffer. *Protein Expr Purif* 32, 83-88.

Chen, Y.H., and Yang, J.T. (1971). A new approach to the calculation of secondary structures of globular proteins by optical rotatory dispersion and circular dichroism. *Biochem Biophys Res Commun* 44, 1285-1291.

Coureux, P.D., Wells, A.L., Ménétrey, J., Yengo, C.M., Morris, C.A., Sweeney, H.L., and Houdusse, A. (2003). A structural state of the myosin V motor without bound nucleotide. *Nature* 425, 419-423.

Dauter, Z. (2003). Twinned crystals and anomalous phasing. *Acta Crystallogr* D Biol Crystallogr 59, 2004-2016.

DeLano, W. L. (2002) The PyMOL molecular graphics system. *DeLano Scientific* http://www.pymol.org/

DiBella, L.M., and King, S.M. (2001). Dynein motors of the Chlamydomonas flagellum. *Int Rev Cytol* 210, 227-268.

Emsley, P., Lohkamp, B., Scott, W.G., and Cowtan, K. (2010). Features and development of Coot. *Acta Crystallogr* D Biol Crystallogr 66, 486-501.

Essmann, U., Perera, L., Berkowitz, M.L., Darden, T., Lee, H., Pedersen, L.G., (1995). A smooth particle mesh Ewald method. *J Chem Phys* 103:8577–93.

French, S., Wilson, K. (1978). On the Treatment of Negative Intensity Observations *Acta Crystallogr* A 34, 517-525.

Fukuda, I., Kamiya, N., Yonezawa, Y., and Nakamura, H. (2012). Simple and accurate scheme to compute electrostatic interaction: zero-dipole summation technique for molecular system and application to bulk water. *J Chem Phys* 137, 054314.

Fukuda, I., Yonezawa, Y., Nakamura, H. (2011). Molecular dynamics scheme for precise estimation of electrostatic interaction via zero-dipole summation principle. *J Chem Phys* 134:164107.

Fukunishi, Y., Mikami, Y., Nakamura, H. (2003). The filling potential method: a method for estimating the free energy surface for protein–ligand docking. *J Phys Chem* B 107:13201–10.

Gibbons, I.R. (1981). CILIA AND FLAGELLA OF EUKARYOTES. *Journal of Cell Biology* 91, S107-S124.

Gibbons, I.R., Garbarino, J.E., Tan, C.E., Reck-Peterson, S.L., Vale, R.D., and Carter, A.P. (2005). The affinity of the dynein microtubule-binding domain is modulated by the conformation of its coiled-coil stalk. *J Biol Chem* 280, 23960-23965.

Hafezparast, M., Klocke, R., Ruhrberg, C., Marquardt, A., Ahmad-Annuar, A., Bowen, S., Lalli, G., Witherden, A.S., Hummerich, H., Nicholson, S., et al. (2003). Mutations in dynein link motor neuron degeneration to defects in retrograde transport. *Science* 300, 808-812.

Höök, P., Mikami, A., Shafer, B., Chait, B.T., Rosenfeld, S.S., and Vallee, R.B. (2005). Long range allosteric control of cytoplasmic dynein ATPase activity by the stalk and C-terminal domains. *J Biol Chem* 280, 33045-33054.

Immirzi, A. (1973). A general Fourier program for X-ray crystal-structure analysis which utilizes the Cooley-Tukey algorithm. *J. Appl. Cryst*. 6, 246-249.

Kabsch, W., and Sander, C. (1983). Dictionary of protein secondary structure: pattern recognition of hydrogen-bonded and geometrical features. *Biopolymers* 22, 2577-2637.

Jorgensen, W.L., Chandrasekhar, J., Madura, J.D., Impey, R.W., Klein, M.L. (1983). Comparison of simple potential functions for simulating liquid water. *J Chem Phys* 79:926–35.

Joung, I.S., and Cheatham, T.E. (2008). Determination of alkali and halide monovalent ion parameters for use in explicitly solvated biomolecular simulations. *J Phys Chem* B 112, 9020-9041.

Kamiya, N., Fukuda, I., Nakamura, H. (2013). Application of zero-dipole summation method to molecular dynamics simulations of a membrane protein system. *Chem Phys* Lett 568–569:26–32.

Kamiya, N., Watanabe, YS., Ono, S., Higo J. (2005). AMBER-based hybrid force field for conformational sampling of polypeptides. *Chem Phys* Lett 401:312–7.

Karki, S., and Holzbaur, E.L.F. (1999). Cytoplasmic dynein and dynactin in cell division and intracellular transport. *Current Opinion in Cell Biology* 11, 45-53.

Kon, T., Imamula, K., Roberts, A.J., Ohkura, R., Knight, P.J., Gibbons, I.R., Burgess, S.A., and Sutoh, K. (2009). Helix sliding in the stalk coiled coil of dynein couples ATPase and microtubule binding. *Nat Struct Mol Biol* 16, 325-333.

Kon, T., Mogami, T., Ohkura, R., Nishiura, M., and Sutoh, K. (2005). ATP hydrolysis cycle-dependent tail motions in cytoplasmic dynein. *Nat Struct Mol Biol* 12, 513-519.

Kon, T., Nishiura, M., Ohkura, R., Toyoshima, Y.Y., and Sutoh, K. (2004). Distinct functions of nucleotide-binding/hydrolysis sites in the four AAA modules of cytoplasmic dynein. *Biochemistry* 43, 11266-11274.

Kon, T., Oyama, T., Shimo-Kon, R., Imamula, K., Shima, T., Sutoh, K., and Kurisu, G. (2012). The 2.8 Å crystal structure of the dynein motor domain. *Nature* 484, 345-350.

Kon, T., Sutoh, K., and Kurisu, G. (2011). X-ray structure of a functional full-length dynein motor domain. *Nat Struct Mol Biol* 18, 638-642.

Koonce, M.P., and Samsó, M. (1996). Overexpression of cytoplasmic dynein's globular head causes a collapse of the interphase microtubule network in Dictyostelium. *Mol Biol Cell* 7, 935-948.

Kozielski, F., Sack, S., Marx, A., Thormählen, M., Schönbrunn, E., Biou, V., Thompson, A., Mandelkow, E.M., and Mandelkow, E. (1997). The crystal structure of dimeric kinesin and implications for microtubule-dependent motility. *Cell* 91, 985-994.

Kull, F.J., Sablin, E.P., Lau, R., Fletterick, R.J., and Vale, R.D. (1996). Crystal structure of the kinesin motor domain reveals a structural similarity to myosin. *Nature* 380, 550-555.

Kull, F.J., Vale, R.D., and Fletterick, R.J. (1998). The case for a common ancestor: kinesin and myosin motor proteins and G proteins. *J Muscle Res Cell Motil* 19, 877-886.

Kunau, W.H., Beyer, A., Franken, T., Götte, K., Marzioch, M., Saidowsky, J., Skaletz-Rorowski, A., and Wiebel, F.F. (1993). Two complementary approaches to study peroxisome biogenesis in Saccharomyces cerevisiae: forward and reversed genetics. *Biochimie* 75, 209-224.

Lovell, S.C., Davis, I.W., Arendall, W.B., de Bakker, P.I., Word, J.M., Prisant, M.G., Richardson, J.S., and Richardson, D.C. (2003). Structure validation by Calpha geometry: phi,psi and Cbeta deviation. *Proteins* 50, 437-450.

Mallik, R., and Gross, S.P. (2004). Molecular motors: strategies to get along. *Curr Biol* 14, R971-982.

Mashimo, T., Fukunishi, Y., Kamiya, N., Takano, Y., Fukuda, I., Nakamura, H. (2013). Molecular dynamics simulations accelerated by GPU for biological macromolecules with a non-Ewald scheme for electrostatic interactions. *J Chem Theory Comput* 9:5599–609.

Matthews, B.W. (1968). Solvent content of protein crystals. *J Mol Biol* 33, 491-497.

McNaughton, L., Tikhonenko, I., Banavali, N.K., LeMaster, D.M., and Koonce, M.P. (2010). A low affinity ground state conformation for the Dynein microtubule binding domain. *J Biol Chem* 285, 15994-16002.

Mizuno, N., Narita, A., Kon, T., Suto, K., and Kikkawa, M. (2007). Cryo-EM study of dynein-microtubule complex. *Biophysical Journal,* 495A-496A.

Neuwald, A.F., Aravind, L., Spouge, J.L., and Koonin, E.V. (1999). AAA+: A class of chaperone-like ATPases associated with the assembly, operation, and disassembly of protein complexes. *Genome Res* 9, 27-43.

Otwinowski, Z., Minor, W., (1997) Processing of X-ray diffraction data collected in oscillation mode. *Methods Enzymol* 276:307–26.

Pettersen, E.F., Goddard, T.D., Huang, C.C., Couch, G.S., Greenblatt, D.M., Meng, E.C., and Ferrin, T.E. (2004). UCSF Chimera--a visualization system for exploratory research and analysis. *J Comput Chem* 25, 1605-1612.

Read, R.J. (1986). Improved Fourier coefficients for maps using phases from partial structures with errors *Acta Crystallogr* A 42, 140-149.

Redwine, W.B., Hernández-López, R., Zou, S., Huang, J., Reck-Peterson, S.L., and Leschziner, A.E. (2012). Structural basis for microtubule binding and release by dynein. *Science* 337, 1532-1536.

Roberts, A.J., Numata, N., Walker, M.L., Kato, Y.S., Malkova, B., Kon, T., Ohkura, R., Arisaka, F., Knight, P.J., Sutoh, K., et al. (2009). AAA+ Ring and linker swing mechanism in the dynein motor. *Cell* 136, 485-495.

Ryckaert, J-P., Ciccotti, G., Berendsen, H.J.C. (1977). Numerical interaction of the Cartesian equations of motion of a system with constraints: molecular dynamics of *n*-alkanes. *J Comput Phys* 23:327–41.

Sakakibara, H., Kojima, H., Sakai, Y., Katayama, E., and Oiwa, K. (1999). Inner-arm dynein c of Chlamydomonas flagella is a single-headed processive motor. *Nature* 400, 586-590.

Schmidt, H., Gleave, E.S., and Carter, A.P. (2012). Insights into dynein motor domain function from a 3.3-Å crystal structure. *Nat Struct Mol Biol* 19, 492-497, S491.

Strelkov, S.V., and Burkhard, P. (2002). Analysis of alpha-helical coiled coils with the program TWISTER reveals a structural mechanism for stutter compensation. *J Struct Biol* 137, 54-64.

Studier, F.W. (2005). Protein production by auto-induction in high density shaking cultures. *Protein Expr Purif* 41, 207-234.

TenEyck, L.F. (1972). Crystallographic Fast Fourier Transforms. *Acta Crystallogr* A 29, 183-191.

Ten Eyck, L.F. (1985). Fast Fourier transform calculation of electron density maps. *Methods Enzymol* 115, 324-337.

Terwilliger, T.C., Adams, P.D., Read, R.J., McCoy, A.J., Moriarty, N.W., Grosse-Kunstleve, R.W., Afonine, P.V., Zwart, P.H., and Hung, L.W. (2009). Decision-making in structure solution using Bayesian estimates of map quality: the PHENIX AutoSol wizard. *Acta Crystallogr* D Biol Crystallogr 65, 582-601.

Vale, R.D. (2003). The molecular motor toolbox for intracellular transport. *Cell* 112, 467-480.

Walshaw, J., and Woolfson, D.N. (2001). SOCKET: A program for identifying and analysing coiled-coil motifs within protein structures. *Journal of Molecular Biology* 307, 1427-1450.

Waters, A.M., and Beales, P.L. (2011). Ciliopathies: an expanding disease spectrum. *Pediatr Nephrol* 26, 1039-1056.

Yang, J., Xu, C., Wang, C., and Kopecek, J. (2006). Refolding hydrogels self-assembled from N-(2-hydroxypropyl)methacrylamide graft copolymers by antiparallel coiled-coil formation. *Biomacromolecules* 7, 1187-1195.

Yaremchuk, A.D., Tukalo, M.A., Krikliviy, I., Malchenko, N., Biou, V., Berthet-Colominas, C., and Cusack, S. (1992). A new crystal form of the complex between seryl-tRNA synthetase and tRNA(Ser) from Thermus thermophilus that diffracts to 2.8 A resolution. *FEBS* Lett 310, 157-161.

Zhao, X., Ghaffari, S., Lodish, H., Malashkevich, V.N., and Kim, P.S. (2002). Structure of the Bcr-Abl oncoprotein oligomerization domain. *Nat Struct Biol* 9, 117-120.

## List of publications

Nishikawa, Y., Oyama, T., Kamiya, N., Kon, T., Toyoshima, Y.Y., Nakamura, H., Kurisu, G. (2014) Structure of the entire stalk region of the Dynein motor domain. *J. Mol. Biol.*, **426:** 3232-3245